Remote Sensing of Environment 263 (2021) 112540

Contents lists available at ScienceDirect

Remote Sensing of Environment

journal homepage: www.elsevier.com/locate/rse

# Influence of flight parameters on UAS-based monitoring of tree height, diameter, and density

Neal C. Swayze [a], Wade T. Tinkham [a,*], Jody C. Vogeler [b], Andrew T. Hudak [c]

[a] Department of Forest and Rangeland Stewardship, Colorado State University, Fort Collins, CO 80524-1472, USA
[b] Natural Resource Ecology Laboratory, Colorado State University, Fort Collins, CO 80523-1499, USA
[c] USDA Forest Service, Rocky Mountain Research Station, Moscow, ID 83844, USA

A R T I C L E I N F O

Editor name: Jing M. Chen.

*Keywords:*
Tree detection
Canopy height model
Forest inventory
Unmanned aerial system
Forest structure

A B S T R A C T

Increased focus on restoring forest structural variation and spatial pattern in dry conifer forests has led to greater emphasis on forest monitoring strategies that can be summarized across scales. To inform restoration objectives with data sources that can characterize individual trees, groups of trees, and the entire stand, different remote sensing strategies such as aerial and terrestrial light detection and ranging (LiDAR) have been explored. Unfortunately, high equipment and operational costs of aerial systems, along with limited spatial extent of terrestrial scanners, have restricted widespread adoption of these technologies for repeated forest monitoring. This study investigates applications of unmanned aerial system (UAS) imagery for Structure from Motion derived modeling of individual tree and stand-level metrics. Specifically, we evaluate how flight parameters impact UAS extracted height and imputed DBH accuracies against field stem-mapped values. In total, 30 UAS image datasets collected from combinations of three altitudes, two flight patterns, and five camera orientations were assessed. Tree heights were extracted using a variable window function that searched UAS-derived canopy height models, while DBH was sampled from point cloud slices at 1.32–1.42 m using a least squares circle fitting algorithm. The sample trees were then filtered against National Forest Inventory data from the study region to ensure reasonable matching of extracted heights and diameters. The matched values were used to create a height to diameter relationship for predicting missing DBH values. Extracted and imputed tree values were compared against stem-mapped values to determine tree commission and omission rates, the accuracy and precision of extracted tree height, DBH, as well as overstory and understory stand density. Finding that, 1) tree extraction accuracy and correctness was maximized (F-score = 0.77) for nadir crosshatch UAS flight designs; 2) extracted tree height $R^2$ with stem-mapped values was high ($R^2 \geq 0.98$) for all UAS flight parameters, but the quality (mean error = 0.79 cm) and quantity (~10% of all trees) of extracted DBH values was maximized for lower altitude, nadir crosshatch acquisitions; 3) the distribution of predicted DBH values most closely matched field observed values for off-nadir crosshatch flight designs; 4) using either off-nadir or crosshatch flight designs at lower altitudes maximized correlation ($r > 0.70$) and accuracy (basal area within 2 $m^2$ $ha^{-1}$) of stand density estimates. This study demonstrates a novel UAS-based inventory strategy for estimating individual tree structural attributes (i.e., location, height, and DBH) in dry conifer forests, without the need for in situ field observations.

## 1. Introduction

The increasing focus on restoration of forest structural variation and spatial pattern (Tinkham et al., 2017; Addington et al., 2018) in dry conifer forests has led to a greater emphasis on forest monitoring strategies that can be summarized across scales (Cannon et al., 2018). At fine spatial scales, restoration objectives in these forested systems emphasize creating a variable matrix of groups and openings, while also reducing the prevalence of small trees that have established in the absence of an intact frequent fire regime (Allen et al., 2002). Promoting variable density tree groups with openings between groups can increase forest resilience to fire (Ziegler et al., 2017a). Fine scale restoration

* Corresponding author at: Department of Forest and Rangeland Stewardship, Colorado State University, 1472 Campus Delivery, Fort Collins, CO 80524-1472, USA.

*E-mail addresses:* Neal.Swayze@colostate.edu (N.C. Swayze), Wade.Tinkham@colostate.edu (W.T. Tinkham), Jody.Vogeler@colostate.edu (J.C. Vogeler), Andrew.Hudak@usda.gov (A.T. Hudak).

https://doi.org/10.1016/j.rse.2021.112540
Received 20 December 2020; Received in revised form 27 March 2021; Accepted 28 May 2021

objectives also include retention of dense groups and patches of older trees for tree squirrels, snags for woodpeckers and secondary-cavity nesting species, and logs for invertebrate species and small mammals (Reynolds et al., 2013). At broader spatial scales, restoring heterogeneity within stands and in-between stands is critical for moving dry conifer forest systems towards historical conditions that balanced resilience to disturbance with providing a diversity of habitat structures (North et al., 2009). To inform these restoration objectives with data sources that can be summarized across scales from groups of trees to entire stands, different strategies such as light detection and ranging (LiDAR) have been explored.

In the past 30 years, research focused on forest structure modeling has investigated using both aerial LiDAR (ALS) and terrestrial LiDAR (TLS) to acquire three-dimensional point returns to estimate first-order properties like a tree's location, height, and stem diameter (Hopkinson et al., 2004; You et al., 2016), as well as derive second-order properties like basal area and timber volume per hectare (Nilsson, 1996; Tinkham et al., 2016). ALS datasets commonly range from 0.5–40 points $m^{-2}$ and have been widely tested across a range of forest types, densities, and complexities for assessing individual tree characteristics (Wilkes et al., 2015; Kandare et al., 2016). Single tree detection accuracies from ALS point cloud-derived canopy height models (CHM) range from 40 to 94%, with detection rates decreasing as forest complexity and density increase (Falkowski et al., 2006; Silva et al., 2016; Sačkov et al., 2019). Most omitted trees from these techniques tend to occupy lower portions of the forest canopy where they are partially/fully occluded by the crowns of taller trees. The use of TLS is newer in the field of forestry but can provide ultra-high density (25–100 thousand points $m^{-2}$; Saarinen et al., 2017) point clouds for sampling individual trees or plots. Despite limited spatial extent, TLS observations are now an established forest sampling tool with many studies highlighting the technological potential for characterizing individual tree stem characteristics. TLS has been found to detect 20 to >90% of trees, with accuracies varying across forest density and scan design (Maas et al., 2008; Heinzel and Huber, 2016); various stem extraction methods have been shown to achieve diameter at breast height (DBH; 1.37 m) precisions of 1.5–3.5 cm RMSE. When applied together, the fusion of ALS spatial extent and TLS resolution has been able to generate comprehensive structural data of forest stands (Paris et al., 2017). Unfortunately, the high equipment and operational costs of ALS, along with limited TLS spatial extent, have restricted their widespread adoption in forest monitoring (Cook, 2017). This highlights a need for more cost and time efficient methods of acquiring tree level overstory and understory forest structural characteristics to inform management strategies.

The same techniques developed for characterizing individual trees in ALS and TLS point clouds are finding new applications with LiDAR sensors mounted on unmanned aerial systems (UAS; Brede et al., 2017; Sankey et al., 2017; Dalla Corte et al., 2020; Neuville et al., 2021). These UAS-LiDAR systems are actively undergoing development for direct characterization of individual trees to fill an intermediate spatial extent between ALS and TLS systems. Attempts to extract DBH values from UAS-LiDAR datasets have ranged from 18 to 82% of trees, with comparisons to field observed DBHs having correlations of 0.24 to 0.98 and RMSE of 3.46 to 25.0 cm (Brede et al., 2017; Dalla Corte et al., 2020; Neuville et al., 2021). This wide range in DBH extraction success follows a gradient in forest complexity and differences in acquisition parameters, with leaf-on conditions in deciduous forest systems causing large increases in errors. Common UAS systems can cost $1,000–20,000 with compatible LiDAR systems costing $70,000-95,000, but this active area of development is driving competition with proposed LiDAR systems that have not been thoroughly tested costing closer to $25,000 (Torresan et al., 2018).

Similar estimations of tree locations, height, and DBH have been attempted through structure from motion (SfM) photogrammetry, which uses a camera's properties and different image viewpoints to solve for the three-dimensional location of co-occurring pixels (Forsman et al., 2016). Testing of terrestrial SfM for stem detection has found similar detection rates to TLS, with small stand (<100 trees) demonstrations extracting 60%–98% of tree locations (Liang et al., 2014; Mokroš et al., 2018). Additionally, terrestrial SfM DBH measurement precision only decreases slightly over TLS to 5.1–7.2 cm RMSE (Forsman et al., 2016; Piermattei et al., 2019). The low cost of UAS has made applying SfM to imagery collected above the forest canopy a viable alternative to ALS (Dandois and Ellis, 2013; Thiel and Schmullius, 2016).

Improving sensor technology has enabled UAS-SfM point clouds with data densities in excess of 1000 points $m^{-2}$ (Creasy et al., 2021). These high data densities enable generation of finer resolution CHMs compared to ALS, improving detection rates of suppressed and intermediate trees. In some instances, secondary forest parameters like basal area have been modeled from extracted tree densities based on local relations between density and basal area (Belmonte et al., 2020). The relatively high precision of these efforts suggests these strategies could be applied to monitor dry conifer forest restoration objectives. The rapidly expanding use of SfM-based photogrammetry in forestry is a ripe area for evaluating how UAS image acquisition strategies impact derived estimates of forest structure. Early exploration of flight parameters has focused on how photo overlap, flight height, and ground sampling distance impact image alignment and point cloud reconstruction quality (Dandois et al., 2015; Nesbit and Hugenholtz, 2019). While research has started to evaluate how flight parameters impact structural measurements like tree height and crown diameter (Frey et al., 2018), knowledge gaps remain regarding other structural attributes. Particularly, the impacts of UAS flight altitude and pattern along with camera angle (Fig. 1) have received little attention for their implications on individual tree parameter assessment.

Most UAS forest photogrammetry studies utilize conventional serpentine flight patterns (Fig. 1A) and nadir (0° or perpendicular to the ground; Fig. 1D) camera view angles for generating point clouds. Nesbit and Hugenholtz (2019) found that creating a crosshatch flight (Fig. 1C) by adding a second serpentine flight pattern (Fig. 1B) of off-nadir (20–35°) UAS images to a nadir serpentine dataset improved digital terrain model precision. Additionally, adding 15° oblique imagery to nadir imagery datasets in deciduous and coniferous forest leaf-on and leaf-off conditions increased understory point cloud density (Díaz et al., 2020). The use of off-nadir 45° camera angles provided reliable stem reconstruction of ~70% of trees in a leaf-off deciduous forest (Fritz et al., 2013); however, the authors speculated that altering the camera orientation during crosshatch flight paths to provide a diversity of camera orientations could further improve stem identification and DBH extraction. Hybrid SfM photogrammetry approaches that utilize both UAS and terrestrially collected images can provide RMSE of less than 1 cm and 1 m for tree DBH and height, respectively (Mikita et al., 2016). While being highly precise, the smaller extent of terrestrial image collection limits such direct tree observations through data fusion.

Since preliminary testing of crosshatch and off-nadir UAS data acquisition methods indicate improved point density in the lower canopy and stem region (Díaz et al., 2020), it is logical to more thoroughly investigate the impact of these variables on extracted tree parameters like DBH. However, as it is unlikely UAS point clouds generated from images acquired above the forest canopy will directly characterize DBH of all trees, other techniques of filling missing DBH values are needed in order to directly summarize basal area or apply common allometries of tree volume and biomass. Imputation of missing values in forest inventories commonly occurs by using paired DBH and height values to calibrate regional relationships of DBH predicting height in order to fill in missing heights within the inventory (Weiskittle et al., 2011). Similarly, these regional relationships have been directly applied to predict DBH from remotely sensed height for tree biomass estimation (Tinkham et al., 2016). Merging these strategies to ensure correctly extracted DBH and height observations from UAS point clouds meet regional expectations could enable reliable prediction of missing DBH values without the need for in situ observations.

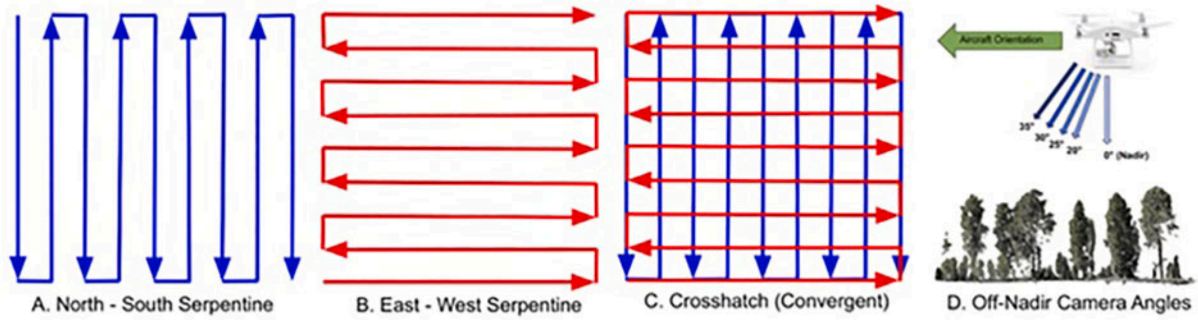


**Fig. 1.** Flight pattern for N-S serpentine (A), *E*-W serpentine (B), crosshatch (C) and camera orientation along a flight line depicting multiple camera angle scenarios (D).

This study investigates the influence of UAS flight parameters on modeling individual tree and stand-level metrics from UAS developed height to DBH relationships through a series of tasks. First, we evaluate the impact of UAS flight altitude, camera angle, and flight path on UAS CHM individual tree detection rates and UAS-SfM point cloud extracted tree height and DBH accuracy. Next, a regional height to DBH relationship is applied to filter UAS extracted tree height and DBH observations, which are then used to develop a local height to DBH model to predict missing UAS DBH values. Finally, we evaluate the effect of flight parameters on the precision of plot and stand level estimates of overstory (>5 m tall) basal area (m$^2$ ha$^{-1}$) and trees per hectare, along with understory trees per hectare.

## 2. Methods

The study workflow (Fig. 2) consisted of four components: 1) data collection, 2) tree extraction, 3) data filtering and modeling, and 4) analysis and validation of model output. First, UAS imagery and stem map data collected in the field. Second, UAS imagery was processed to generate point clouds and CHMs. Third, tree heights and DBHs were extracted from UAS datasets. These extracted heights and DBHs were spatially paired, filtering against a regional height to DBH relationship, and used to model missing DBH values. Fourth, commission and omission errors were calculated for extracted trees, and the accuracy and precision of tree height, DBH, and overstory and understory stand density.

### 2.1. Study area and field data

This study was conducted in the Manitou Experimental Forest, about 40 km northwest of Colorado Springs, Colorado. A 1 ha (100 × 100 m) stem map of ponderosa pine (*Pinus ponderosa* var. *scopulorum* Dougl. Ex Laws.) dominated forest was established for validation (Fig. 3). All trees >1.37 m tall ($n$ = 890) were mapped and inventoried using a grid of survey points distributed across the site with observations of tree height and DBH recorded in August 2018. The site exhibits a multi-aged forest structure, due to regeneration pulses following a shelterwood style harvest in the 1880's and pine beetle disturbance in the 1980's (Boyden et al., 2005). The inventory demonstrates a stand structure with increased density beyond historical levels within the region (Battaglia et al., 2018), with enough overstory shading to allow five Douglas-fir (*Pseudotsuga menziesii* (Mirb.) Franco var. *glauca* (Beissn.) Franco) and two blue spruce (*Picea pungens* Engelm.) to establish in the understory. The shade intolerance of ponderosa pine and the systems disturbance regime typically lead stands to develop a matrix of spatially aggregated tree clumps of a single age group (±10–20 year) that are all similar in height (Ziegler et al., 2017b). Similar spatial partitioning of tree sizes can be seen within the study site datasets (Fig. 3). Dividing the stand into two strata at a 5 m tall breakpoint shows 374 trees ha$^{-1}$ and 24.32 m$^2$ ha$^{-1}$ of basal area in the overstory tree stratum (5 to ~25 m tall) and 516 trees ha$^{-1}$ in the understory tree stratum (< 5 m tall; see inset of tree size distributions in Fig. 2). We selected the 5 m threshold as it roughly corresponds to a 10 cm DBH, a common regional forest inventory breakpoint for describing overstory and understory forest densities,

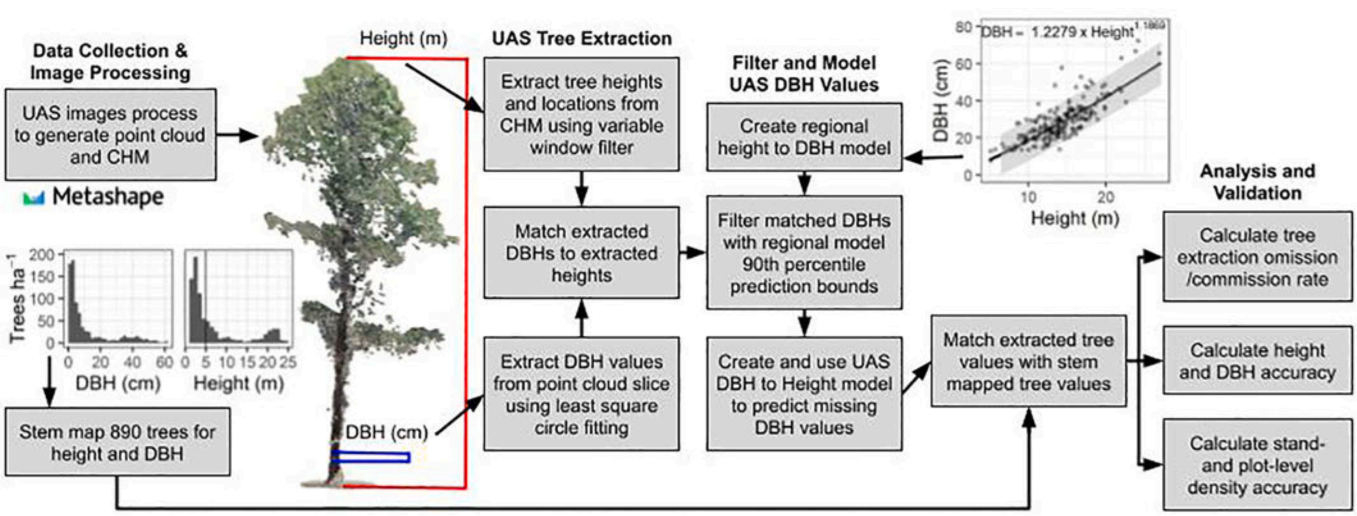


**Fig. 2.** Integrative workflow of the data collection and processing, tree matching, and analysis steps used to assess accuracy of UAS extracted tree- and stand-level characteristics. (2-column figure).

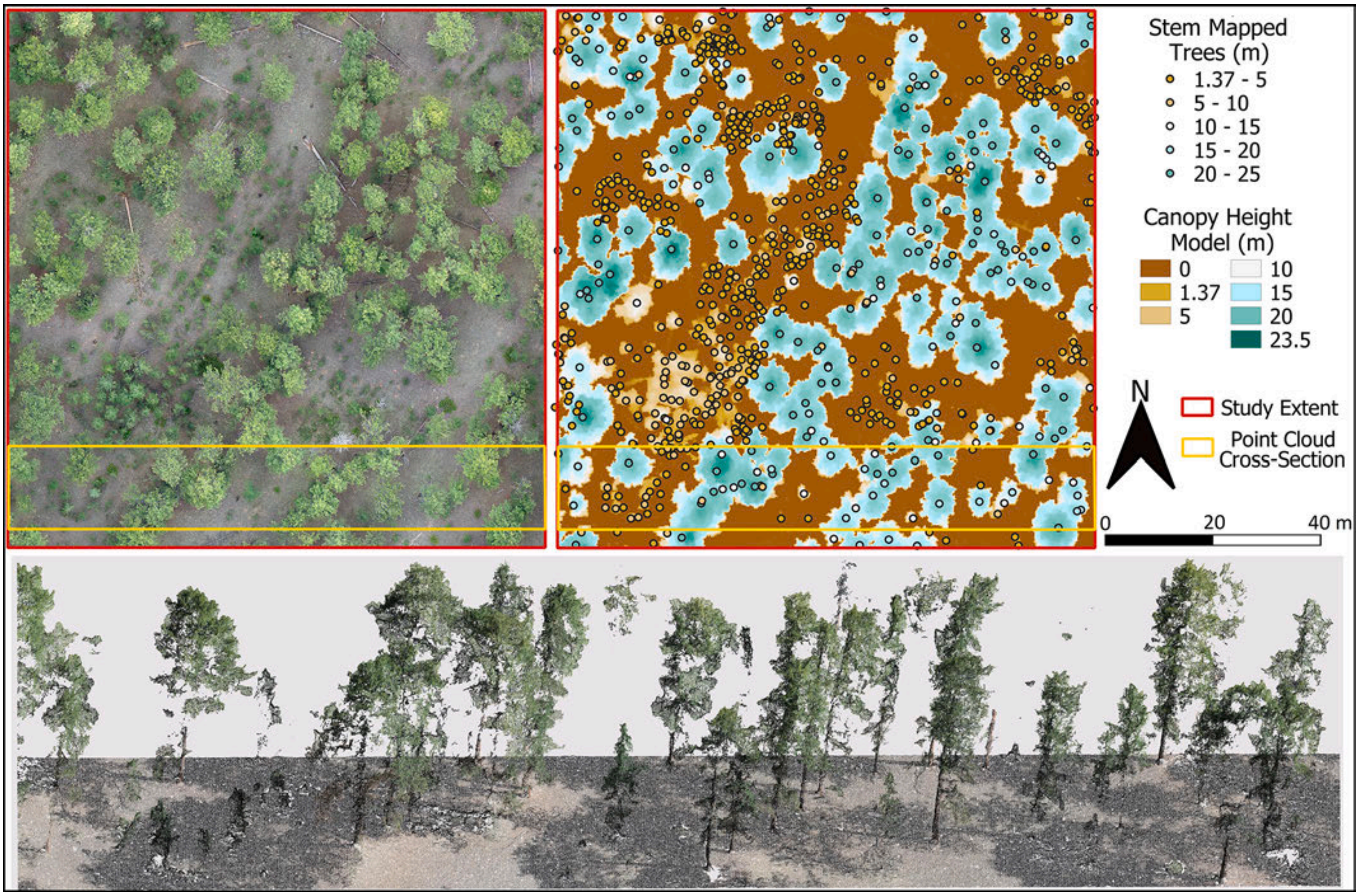


**Fig. 3.** Study area shown in the top row with 2.1 cm resolution orthomosaic image and 10 cm resolution canopy height model both generated from 90 m altitude UAS serpentine acquisition with nadir camera angle. Maps are overlaid with stem mapped trees to portray tree spatial arrangement and alignment with UAS data. Bottom row shows oblique view of SfM point cloud cross-section (15 × 100 m) for the bounding box overlaid on the maps. (2-column figure).

where the understory includes what is commonly referred to as sapling or advanced regeneration.

### 2.2. Regional field data

For development of a regional height to DBH relationship, we acquired USA Forest Service Forest Inventory and Analysis (FIA) data (Tinkham et al., 2018) for 6693 plots in the state of Colorado. We filtered plots to only retain those containing >70% ponderosa pine basal area and with a site index within ±2 m of the study area's site index, leaving 92 plots with 196 trees. We fit a power function to predict DBH as a function of height using the nlme package (Pinheiro et al., 2018) in the R statistical program. We generated 90th percentile prediction bounds for the model (see inset model graph in Fig. 2) to filter UAS extracted DBH values that were matched with UAS extracted heights.

### 2.3. UAS image collection

We conducted a total of 30 UAS flights over the 1 ha study area in July 2019, collecting approximately 7140 images in 4.66 h of in-air flight time. The imagery was collected with a Da-Jiang Innovations (DJI) Phantom 4 Pro UAS, with a 1 in. 20 MP (5472 × 3648 pixels) metal oxide semiconductor red-green-blue (RGB) sensor at a fixed 8.8 mm focal length. Flights were conducted at three altitudes above ground level (65, 90, and 115 m). Images were captured over a 110 × 110 m size grid centered on the 1 ha study area with 90% front and side overlap at a speed of 4 m sec$^{-1}$ to accommodate the systems minimum interval of 2 s between image captures. The sensor captured images in jpeg format using a manual focus set to infinity, image dimensions set to 3:2, apertures ranging from 4.0–5.6 (F-stop), shutter speeds ranging from 1/100th - 1/500th of a second, and an ISO value of 100. Altizure (version 4.6.8.193; Shenzhen, China) for Apple iOS was used to acquire nadir imagery using separate North-South (NS) and East-West (EW) camera orientations at each altitude for a total of six nadir image acquisitions. Then Pix4D Capture (Pix4D S.A., Laussanne, Switzerland) was used to acquire off-nadir imagery (20, 25, 30, and 35°) using separate NS and EW camera orientations at each altitude, a total of 24 off-nadir acquisitions. These off-nadir camera angels were utilized based on previous observations by Nesbit and Hugenholtz (2019) who found this range of angles minimized distortion errors in digital elevation models.

### 2.4. UAS image SfM processing and filtering

We utilized Agisoft Metashape to process the imagery from the 30 flights following the workflow outlined by Tinkham and Swayze (2021). This was done by first finding matching tie points and aligning the photos, generating the sparse point cloud, georeferencing the imagery, and then creating dense RGB point clouds. These consisted of 15 serpentine NS and 15 crosshatch SfM point clouds distributed across three altitudes and five camera angles. The Metashape SfM processing included ten ground control points collected using a Trimble GeoXT (Trimble Inc., Sunnyvale, CA, USA) with SBAS real-time correction accuracies of <1 m. Camera lens calibration was automatically completed during the align photos step, with generic preselection enabled, reference preselection set to source, and adaptive camera model fitting enabled. Post-image alignment, ground control points were each located in a minimum of thirty images. Geolocation information from the UAS images was disabled, and image alignments were optimized using the focal length (f), principal point coordinates (cx, cy), radial distortion coefficients (k1,k2,k3), and tangential distortion coefficients (p1, p2) with adaptive camera fitting enabled. After manual referencing and image optimization, ground control points with errors greater than 1 m were removed, leaving six final ground control points for the build dense point cloud step. Post-optimization, Metashape reported total XYZ errors ranging from 0.401 to 0.993 m. The build dense cloud step was parameterized with Quality set to High and depth map filtering set to Mild. Previous assessment of Metashape processing parameters in similar forest structures (Tinkham and Swayze, 2021) demonstrated that these setting provide the most accurate reconstructions of all size trees. The full suite of Metashape processing parameters is depicted in Table 1.

After the SfM processing, dense point clouds were filtered to remove erroneous points below ground and above the canopy and classified into ground and non-ground using LAStools version 1.2 (http://lastools.org). Following point filtering and classification, the point clouds were normalized using a 0.25-m resolution DTM interpolated from the classified ground points, and the normalized point clouds were rasterized into 10 cm resolution CHMs. To prepare the SfM point cloud data for DBH extraction, the 30 normalized point clouds were copied into a single "hyper-cloud" file. From the hyper-cloud (900+ million point) vertical sections of the stem (0.5–5 m) and canopy (24–27 m) were extracted to identify a threshold for spectrally identifying stem points. The vertical range of these point cloud slice sizes was decided on to provide relatively pure values of canopy and stem in the hyper-cloud, from these slices 60 random sample locations were then manually extracted using CloudCompare version 2.10.1, visually ensuring that pure stem and canopy points were obtained. The extracted sample points (>800,000 points in each class) were imported into the R statistical programming language (R core Team, 2019) using the lidR package (Roussel and Auty, 2019), where a green:red ratio index (NGRR; Eq. (1)) was calculated on each point to determine the distribution (Fig. 4A) of stem and canopy NGRR values. Based on the distributions, each of the 30 point clouds were segmented to only include points with NGRR values below the 90th percentile of the sample stem points (−0.0152), producing 30 point clouds only containing points with stem reflectance characteristics. For each of these stem point clouds, a 10 cm tall slice (1.32–1.42 m) was extracted and compressed to a height of 1.37 m to represent the DBH region on the trees. An example of this process on a single point cloud stem is displayed in Fig. 4C. These DBH slices were later used to extract individual tree DBH values.

$$NGRR = \frac{DN_{green} - DN_{red}}{DN_{green} + DN_{red}} \tag{1}$$

**Table 1**
Agisoft Metashape processing parameters for SfM photogrammetry reconstruction.

| Parameter | Setting |
|---|---|
| Align Photos | |
| Accuracy | Highest |
| Generic Preselection | Yes |
| Reference Preselection | Source |
| Reset Current Alignment | No |
| Key Point Limit | 40,000 |
| Tie Point Limit | 4000 |
| Apply Mask To | None |
| Exclude Stationary Tie Points | Yes |
| Guided Image Matching | No |
| Adaptive Camera Model Fitting | Yes |
| Optimize Alignment | |
| Fit F | Yes |
| Fit cx, cy | Yes |
| Fit b1, b2 | No |
| Fit K1, K2, K3 | Yes |
| Fit K4 | No |
| Fit p1, p2 | Yes |
| Fit Additional Corrections | No |
| Adaptive Camera Model Fitting | Yes |
| Build Dense Cloud | |
| Quality | High |
| Reuse depth maps | Yes |
| Depth Filtering | Mild |
| Calculate point colour | Yes |
| Calculate point confidence | No |

### 2.5. Tree location and height extraction

All 30 SfM-derived 10 cm resolution CHMs were analyzed to detect individual tree locations and heights using a local maximum variable window function (Popescu and Wynne, 2004) from the R ForestTools package (Plowright, 2018). The local maximum function searches each CHM to identify local maximum heights within a variable radius moving window based on the rasterized tree heights, assigning a point to locations with defined maximums. The function was parameterized using a linear equation (Eq. (2)) to determine the window radius based on research by Creasy et al. (2021), who found similar parameters for optimizing tree detection across all tree sizes in similar forest systems.

$$variable\ window\ radius = Tree\ Height \times 0.1 \tag{2}$$

where the *variable window radius* is in meters and *Tree Height* is in meters and corresponds to raster cell values in the CHM. The algorithm was parameterized to extract locations and maximum heights of trees >1.37 m tall in the 30 CHMs. The outputs from the tree location and height extraction step included x and y locations paired with a height estimate in meters, here on referred to as extracted tree heights.

### 2.6. Tree DBH extraction

The DBH point cloud slices were analyzed using the R TreeLS package (Conto, 2019), following a workflow presented in Conto et al. (2017). The point cloud slices were rasterized so a Hough Transform circle search algorithm could be used to identify candidate DBH locations with a minimum density setting of 0.001. At each candidate DBH location, a least squares circle fitting algorithm was used on the DBH point cloud slice to estimate DBH. This step utilized a random sample consensus approach to identify points to keep by iteratively fitting least squares circles to candidate DBH locations until the sum of squared distances between the circle and points was minimized, with a tolerance of 0.025 and confidence level of 0.99. For candidate DBH locations that successfully fit a circle, the process generated estimated x and y coordinates and DBH values, here on referred to as extracted tree DBHs.

### 2.7. Matching extracted values with field observations

For each UAS acquisition the extracted tree DBHs were matched with extracted tree heights through a multi-stage filtering process. We first predicted DBH values for each extracted tree height using the regional FIA height to DBH relationship. We then compared FIA predicted DBH values with extracted tree DBHs, identifying matches by iteratively buffering a FIA predicted DBH value using a 4 m radius to account for tree lean and to identify candidate extracted tree DBHs. The candidate extracted tree DBH with the smallest difference to the FIA predicted DBH was assigned to the extracted tree height. Once all extracted tree DBHs had been assigned to an extracted tree height, the paired extracted tree heights and DBHs were filtered to only keep extracted tree DBHs conforming to the 90th percentile prediction bounds of the regional FIA height to DBH relationship. The outputs from the matching and 90th percentile filtering process are here after referred to as paired extracted tree values.

The 30 paired extracted tree value datasets were then each matched with the field observed tree values. After selecting candidate stem map trees within 4 m of a paired extracted tree value, the difference between field observed and extracted tree heights was calculated. The spatial

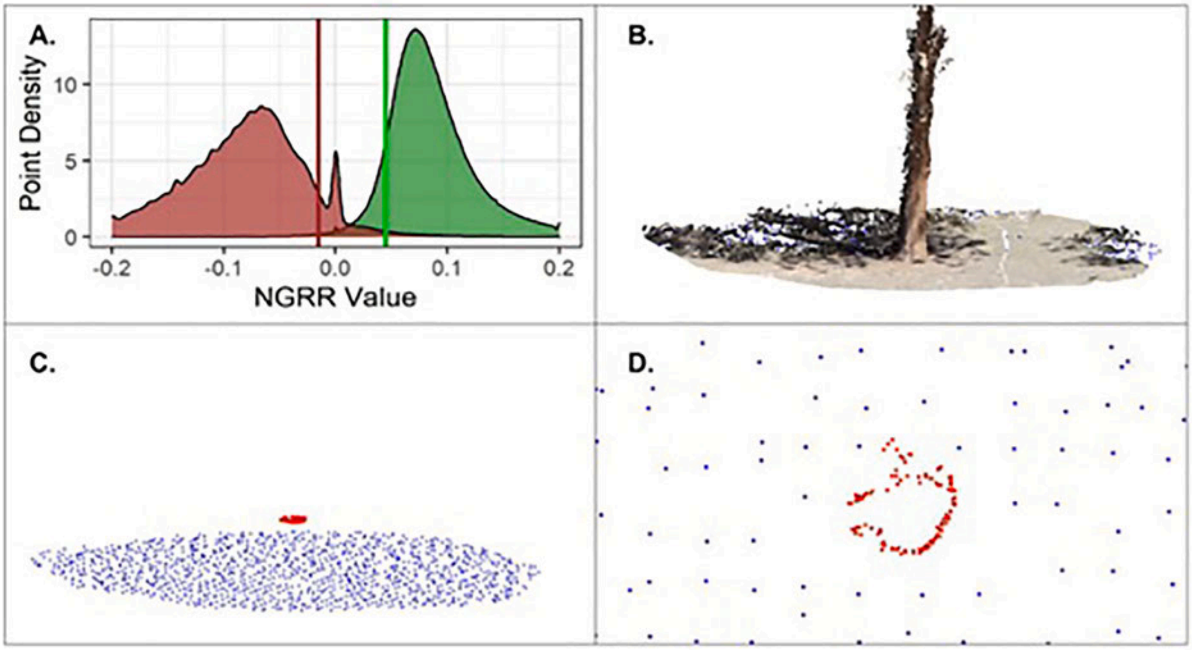


**Fig. 4.** DBH extraction process, showing (A) distributions of stem (brown) and canopy (green) NGRR point values, with vertical lines at the 90th percentile of stem (brown; −0.0152) and 10th percentile of canopy (green; 0.0451), (B) example stem point cloud following NGRR segmentation, (C) 10 cm DBH slice (1.32–1.42 m) with thinned ground points, and (D) top-down view of stem segment with stem points colored red. (1.5-column figure). (For interpretation of the references to colour in this figure legend, the reader is referred to the web version of this article.)

buffer in tree matching was used to account for the effects of tree lean and geolocation errors in both the UAS point clouds and stem mapped tree locations. A successful match required <2 m height error; after a successful match the paired fielded observed and extracted heights were removed from the pool of candidates for further matching. This matching was repeated until all paired extracted tree values were either matched to a stem map tree or were marked as omissions (having no match within 4 m and < 2 m height difference). True Positive, False Negative, and False Positive rates were calculated for paired extracted tree values and stem mapped trees. The quality of each dataset was summarized by calculating recall, precision, and F-score using eqs. (3), (4), and (5), respectively.

$$Recall = \frac{True\ Positive}{True\ Positive + False\ Negative} \tag{3}$$

$$Precision = \frac{True\ Positive}{True\ Positive + False\ Positive} \tag{4}$$

$$F-score = 2 \times \frac{Recall \times Precision}{Recall + Precision} \tag{5}$$

The correctness of the number of extracted trees is described by recall, precision is a measure of extracted tree correctness, and F-score is overall accuracy of the method, which incorporates both precision and recall. In the event of perfect tree extraction, all three metrics would be equal to 1.

### 2.8. DBH prediction and stand parameter estimation

For each dataset, we used the paired extracted tree value estimates of DBH and height to develop a local predictive model of DBH as a function of height using a power equation. We applied these predictive models to the extracted tree heights not matched with an extracted DBH value and merged these with the paired extracted tree values to generate a complete dataset of UAS estimated heights and DBHs for each of the 30 datasets. Mean error (ME) and root mean square error (RMSE) of the final extracted height and DBH values were determined for the 30 SfM extracted datasets to describe the bias and precision of extracted values.

To assess the accuracy of stand-level density metrics, the field observed trees were divided into a 20 × 20 m grid of plots and summarized as trees ha$^{-1}$ (TPH) for trees >5 m tall and ≤6 m tall for each plot and across the entire study area. Additionally, basal area (m$^2$ ha$^{-1}$) was similarly summarized for trees >5 m tall. For each UAS dataset, we also summarized identical TPH and basal area metrics from the paired extracted tree values. We determined correlation and RMSE by comparing the observed and extracted TPH and basal area at the 20 × 20 m plot level, while the absolute error was summarized at the stand level (1 ha) for each metric.

### 2.9. Assessment of altitude, pattern, and camera angle

We used multiple linear regression to determine the influence of tested UAS flight parameters (camera angle, flight altitude, and flight pattern) on tree extraction performance metrics (F-score, precision, and recall). Additional models were generated to describe how flight parameters impacted the correlation, ME, and RMSE of extracted tree heights and DBH values. The main effects of altitude, camera angle, and flight pattern were evaluated for interactions in all regression models through a forward and backward AIC stepwise selection algorithm to determine the best variable subset that minimized the AIC value. In all models, flight pattern was coded as serpentine = 0 and crosshatch = 1. Modeling was performed using the lm and stepAIC functions of the stats (R Core Team, 2019) and MASS R packages (Venables and Ripley, 2002). All main effects were kept in the final model regardless of if they were statistically significant or not.

## 3. Results

### 3.1. Point cloud comparison

Inspection of the point clouds across the different acquisition parameters revealed increased point density at lower altitudes and for the crosshatch flight pattern compared to the serpentine (Table 2). Camera

**Table 2**
Influence of UAS acquisition parameters on the number of images, density of overall, ground, and stem slice points, and horizontal and total alignment error. Letters identify significant ($\alpha = 0.05$) differences within the acquisition parameter using Tukey's HSD test.

| | Images | Overall Points $m^{-2}$ | Ground Points $m^{-2}$ | Stem Slice Points | Horizontal Error (m) | Total Error (m) |
|---|---|---|---|---|---|---|
| All Flights | 242.7 (93.0) | 2272.3 (1351.2) | 15.2 (0.8) | 12,718 (6326) | 0.51 (0.18) | 0.80 (0.13) |
| Flight Patterns | | | | | | |
| Crosshatch | 320.5 (63.4) b | 2627.3 (1545.2) b | 15.4 (0.3) b | 14,055 (5542) | 0.50 (0.17) | 0.81 (0.11) |
| Serpentine | 164.9 (30.8) a | 1917.3 (1060.3) a | 14.9 (1.1) a | 11,381 (6953) | 0.52 (0.19) | 0.80 (0.15) |
| Altitudes | | | | | | |
| 65 | 287.1 (103.1) b | 3961.3 (769.2) c | 15.4 (0.6) | 18,808 (5342) b | 0.42 (0.17) b | 0.79 (0.14) |
| 90 | 215.2 (76.9) a | 1783.7 (455.0) b | 15.3 (0.4) | 9153 (3802) a | 0.40 (0.08) b | 0.80 (0.12) |
| 115 | 225.7 (89.5) a | 1072 (221.4) a | 14.9 (1.1) | 10,193 (4852) a | 0.70 (0.08) a | 0.83 (0.14) |
| Camera Angle | | | | | | |
| 0 | 296.5 (120.3) b | 2598.2 (1417.9) b | 15.8 (0.1) b | 13,225 (5905) | 0.44 (0.13) | 0.67 (0.15) b |
| 20 | 222.8 (75.0) a | 2346.4 (1285.4) ab | 15.4 (0.3) b | 11,548 (4362) | 0.52 (0.16) | 0.80 (0.13) b |
| 25 | 240.3 (101.6) a | 2337.5 (1473.9) ab | 15.3 (0.3) b | 12,948 (4440) | 0.48 (0.18) | 0.81 (0.06) b |
| 30 | 225.3 (76.2) a | 2137.4 (1510.9) ab | 15.2 (0.3) b | 10,473 (6063) | 0.50 (0.20) | 0.85 (0.11) b |
| 35 | 228.3 (97.0) a | 1942.2 (1476.4) a | 14.2 (1.4) a | 15,396 (10,250) | 0.59 (0.24) | 0.90 (0.06) a |

angle also had a general trend of increasing point density as alignment approached nadir. Along with this, the inclusion of crosshatch or off-nadir imagery appears to have increased the vertical range within the point clouds compared to nadir serpentine acquisitions (Fig. 5). Across all acquisitions, there were only minor variations in the density of ground points and stem slice points (Table 2). Ground point density varied from 11.8 to 15.8 points $m^{-2}$, with only small differences identified between the flight patterns and with the 35° camera angle having decreased density compared to the other camera angles. While the count of stem slice points varied from ~3800 to 29,500, only acquisition altitude demonstrated a significant effect with increasing stem points at lower altitudes. Although not significant, visual inspection showed more complete and reliable appearing stem cross-sections in the point cloud for crosshatch and off-nadir acquisitions compared to the base nadir and serpentine acquisition (Fig. 5). Additionally, the Metashape estimated horizontal alignment error was greater for the highest acquisition altitude and although not significant, there was an increasing level of variation the further from nadir the camera angle became (Table 2). Conversely, the total alignment error was not impacted by altitude but did see errors increase as camera angle departed from nadir.

### 3.2. Extracted tree detection performance

Extraction quality metrics (F-score, precision, and recall) for trees

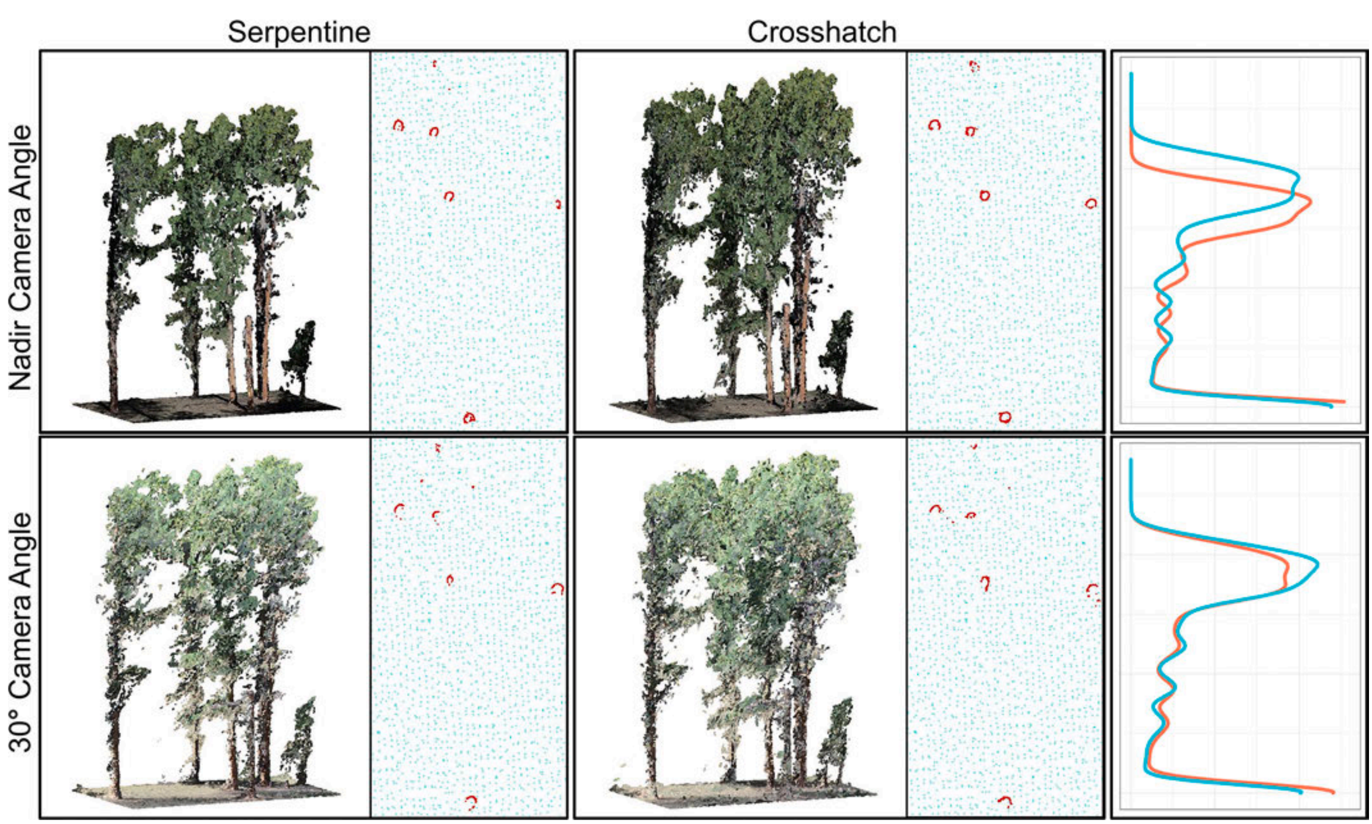


**Fig. 5.** Visualization of serpentine (left) and crosshatch (middle) point clouds from the 65 m acquisitions at nadir (top) and 30° off-nadir (bottom). The point clouds are accompanied by DBH slices where DBH points are colored red and classified ground points are colored blue. Point cloud distributions (right) are shown for the serpentine (red) and crosshatch (blue) acquisitions at the same camera angles. (2-column figure). (For interpretation of the references to colour in this figure legend, the reader is referred to the web version of this article.)

>1.37 m tall varied in their relationship with UAS camera angle and flight pattern according to multiple linear regression (Table 3). Overall performance of correct tree detection and matching as described by F-score was significantly increased by ~4% for crosshatch flight patterns compared to serpentine. F-score values for extracted tree locations varied from 0.429 to 0.771 with a decreasing trend as camera angle increased, with average scores varying from 0.739 to 0.626 for nadir and 35° off-nadir flights, respectively (Fig. 6). Across testing, crosshatch flight patterns paired with nadir camera angles provided the highest SfM tree extraction F-scores.

The proportion of extracted trees that matched field observed trees, summarized as precision, significantly decreased as camera angle increased (Table 3). Average extracted tree location precision varied from 0.942 to 0.669 at nadir and 35° off-nadir (Fig. 6). Capturing the correct number of trees as described by recall only showed weak variation with flight pattern ($P = 0.1010$). Recall for crosshatch flight patterns averaged 0.627 while serpentine patterns averaged 0.59, suggesting crosshatch patterns were slightly closer to the correct number of trees compared to serpentine flights (Fig. 6).

### 3.3. Extracted tree height and DBH assessment

Coefficients of determination between paired extracted tree heights and field observed tree heights exceeded 0.98 for all datasets (Fig. 7). Camera angle and flight pattern both significantly impacted height errors, with nadir camera angles underpredicting by 0.14 m on average, while 20–35° camera angles overpredicted heights by 0.17–0.12 m (Table 4). Crosshatch flight patterns also resulted in increased mean height errors by 0.06 m compared to serpentine patterns. The precision of extracted heights averaged a RMSE of 17.9% for nadir camera angles and significantly increased as camera angle increased from 20 to 35° (Table 4).

Across the 30 datasets, the number of extracted tree DBHs equaled 14.2–47.8% (avg: 31.1%) of the field observed trees. After filtering the extracted tree DBHs with the FIA regional 90th percentile prediction bounds, 4.2–11.5% (avg: 8.0%) were retained as conforming to the expected height to DBH relationship. This translates to 37–103 trees kept for modeling the local height to DBH relationships. Of the tested altitudes, the 65 m flights had a greater proportion of extracted and retained (39.6 and 10.1%, respectively) DBH values following FIA regional filtering compared to higher altitude flights (25.8 and 7.2%, 28.0 and 7.1% for 90 and 115 m, respectively). Similarly, crosshatch flights had greater rates of extraction and filter retained DBH values (avg: 31.9 and 8.4%) compared to serpentine flights (avg: 27.3 and 6.5%).

For all flights the $R^2$ between extracted tree DBHs and field observed values ranged from 0.307 to 0.784. Filtering extracted tree DBHs through the regional FIA relationship improved $R^2$ with field observed DBHs to a range of 0.759 to 0.846 for all UAS datasets. The filtered extracted tree DBH $R^2$were significantly higher for crosshatch flight patterns compared to serpentine flights (Fig. 8), along with significantly increasing $R^2$ as camera angle increased.

For the filtered extracted tree DBHs there was constant overestimation bias that varied with camera angle and flight pattern (Table 4). Nadir acquisition DBH values had a mean error (bias) of 0.79 cm, with this increasing 0.64 cm for every 10° increase in camera angle. Similarly, DBH bias was on average 0.55 cm greater for crosshatch flight patterns compared to serpentine flights. Additionally, the RMSE of extracted and matched DBH values was 41.3% for nadir flight patterns and increased for off-nadir datasets by 8.95% for every 10° increase in camera angle.

**Table 3**
Multiple linear regression of UAS acquisition parameter influence on the reliability of extracted trees, where flight pattern was coded as serpentine = 0 and crosshatch = 1.

| Parameter | Coefficient | Standard Error | t-value | *P*-value | Adj. $R^2$ |
|---|---|---|---|---|---|
| Response = F-score | | | | | 0.1660 |
| Intercept | 0.7942 | 0.0639 | 12.426 | <0.001 | |
| Altitude (m) | −0.0004 | 0.0006 | −0.684 | 0.5002 | |
| Angle (degrees) | −0.0023 | 0.0011 | 1.815 | 0.0811 | |
| Flight Pattern | 0.0337 | 0.0185 | −2.080 | **0.0475** | |
| Response = Precision | | | | | 0.1466 |
| Intercept | 1.0470 | 0.1312 | 7.978 | <0.001 | |
| Altitude (m) | −0.0007 | 0.0013 | −0.536 | 0.5967 | |
| Angle (degrees) | −0.0053 | 0.0022 | −2.373 | **0.0253** | |
| Flight Pattern | 0.0108 | 0.0381 | 0.283 | 0.7796 | |
| Response = Recall | | | | | 0.0655 |
| Intercept | 0.5867 | 0.0449 | 13.064 | <0.001 | |
| Altitude (m) | 0.0001 | 0.0005 | 0.286 | 0.7777 | |
| Angle (degrees) | 0.0006 | 0.0008 | 0.772 | 0.4470 | |
| Flight Pattern | 0.0221 | 0.0130 | 1.700 | 0.1010 | |

Significant parameters (α = 0.05) indicated in boldface.

### 3.4. Distribution of UAS heights and DBHs

Across the datasets, the distributions of paired extracted tree heights closely followed the distribution of field observed heights (Fig. 9). The small underprediction bias present in the nadir serpentine flights (Table 4) carries through during comparison of distributions (Fig. 9). However, crosshatch flight patterns and off-nadir camera angles provided closer visual approximations of the field observed tree height distribution. The distributions of predicted tree DBHs from the UAS relationship between extracted heights and DBHs shows an underrepresentation of smaller diameter trees for serpentine acquisitions (Fig. 9). Visual fit of the distribution for both flight patterns improved for off-nadir camera angles.

### 3.5. UAS basal area and TPH accuracy

Overall, UAS 20 × 20 m plot-level estimates of overstory basal area per hectare, overstory TPH, and understory TPH had high (>0.7) correlation with field observed values, with the exception of acquisitions using 35° off-nadir camera angles where correlations averaged less than 0.5. For overstory basal area per hectare the best acquisitions exceeded correlations of 0.8 and were at lower flight altitudes (65–90 m) with off-nadir camera angles. More than 40% of acquisitions had overstory TPH correlations exceeding 0.8, with the top eight acquisitions also exceeding 0.9 correlations for understory TPH. All the best performing acquisitions for TPH used either crosshatch or off-nadir flight designs.

Camera angle significantly impacted the precision (RMSE) of plot-level estimated overstory (>5 m tall) basal area per hectare and overstory trees per hectare (Fig. 10). Each 10° increase in camera angle resulted in a 3.2 and 6.4% RMSE increase of plot-level overstory TPH and BA, respectively (Table 5). Assessment of basal area for the entire 1 ha study site provided overestimation errors of 1–6 $m^2$ $ha^{-1}$ (or 4.1–24.7%). Study site basal area errors were on average smaller for crosshatch compared to serpentine flight patterns and tended to increase with increased camera angles.

## 4. Discussion

This study evaluated the impact of UAS flight altitude, camera angle, and flight path on: 1) UAS SfM individual tree detection rates; 2) extracted tree height and DBH errors; 3) local UAS-based models to predict individual tree DBH; and 4) estimates of UAS-based plot- and stand-level overstory and understory density metrics. We found that, 1) tree extraction accuracy and correctness was maximized for nadir crosshatch UAS flight designs; 2) extracted tree height precision and accuracy was high for all UAS flight parameters, but the quality and quantity of extracted DBH values was maximized for lower altitude,

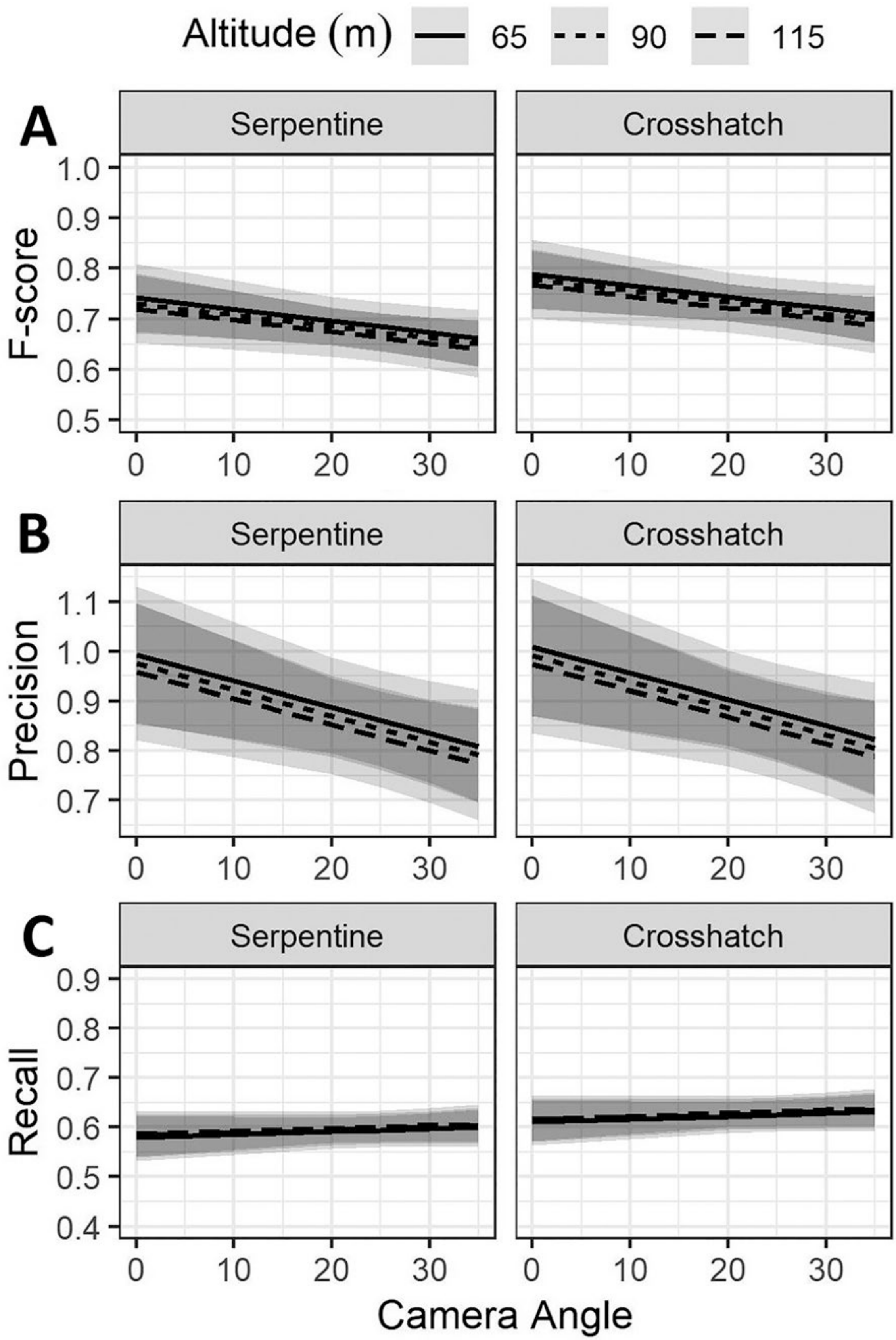


**Fig. 6.** Visualization of multiple linear regression response variables (A) F-score, (B) precision, and (C) recall against predictors of altitude, camera angle, and flight pattern. (1-column figure).

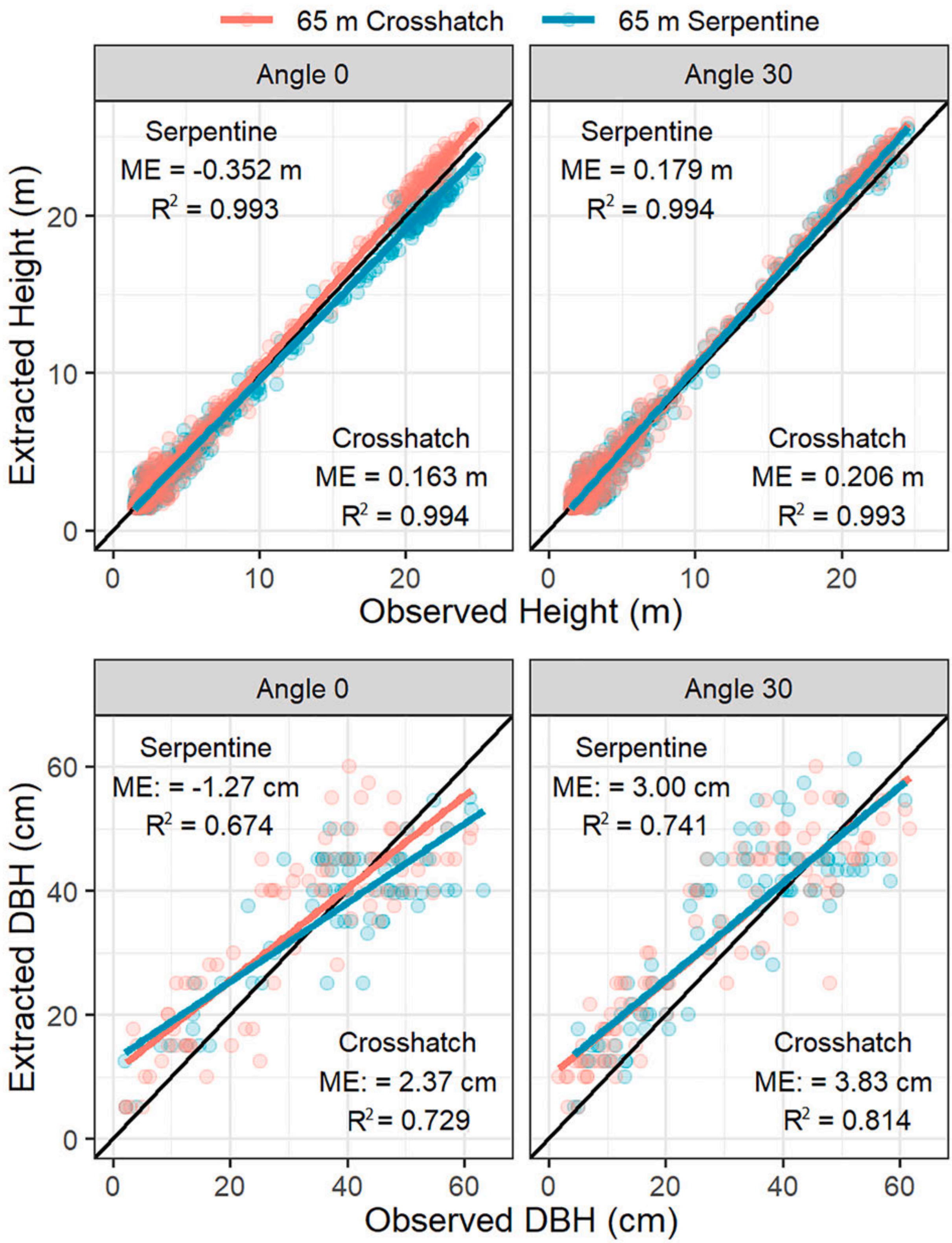


**Fig. 7.** Observed versus extracted height and DBH values for the best serpentine and crosshatch acquisitions (both 65 m altitude). (1-column figure).

nadir crosshatch acquisitions; 3) the distribution of predicted DBH values most closely matched field observed values for off-nadir crosshatch flight designs; 4) the use of either off-nadir or crosshatch flight designs at lower altitudes maximized precision and accuracy of stand density estimates.

### 4.1. Tree location extraction

Our best acquisitions for tree extraction accuracy and correctness (F-score = 0.77) is in the middle of extraction rates found for 30 sites using UAS-based singe tree detection (Mohan et al., 2017). However, our study includes all trees >1.37 m tall whereas most studies only include

**Table 4**
Multiple linear regression of UAS acquisition parameter influence on bias (ME) and precision (RMSE) of extracted tree heights and DBHs meeting FIA 90th percentile prediction bound filtering, where flight pattern was coded as serpentine = 0 and crosshatch = 1.

| Parameter | Coefficient | Standard Error | t-value | *P*-value | Adj. $R^2$ |
|---|---|---|---|---|---|
| Response = Height ME (m) | | | | | 0.4648 |
| Intercept | 0.038 | 0.103 | 0.364 | 0.7189 | |
| Altitude (m) | −0.001 | 0.001 | −1.346 | 0.1900 | |
| Angle (degrees) | 0.008 | 0.002 | 4.668 | **<0.001** | |
| Flight Pattern | 0.064 | 0.030 | 2.140 | **0.0419** | |
| Response = Height RMSE (%) | | | | | 0.1256 |
| Intercept | 15.466 | 1.215 | 12.731 | <0.001 | |
| Altitude (m) | 0.016 | 0.012 | 1.272 | 0.2148 | |
| Angle (degrees) | 0.048 | 0.021 | 2.315 | **0.0287** | |
| Flight Pattern | −0.153 | 0.353 | −0.434 | 0.6679 | |
| Response = DBH ME (cm) | | | | | 0.3555 |
| Intercept | 1.035 | 0.970 | 1.067 | 0.2958 | |
| Altitude (m) | 0.001 | 0.010 | 0.081 | 0.9364 | |
| Angle (degrees) | 0.064 | 0.016 | 3.903 | **<0.001** | |
| Flight Pattern | 0.545 | 0.281 | 1.938 | 0.0635 | |
| Response = DBH RMSE (%) | | | | | 0.0548 |
| Intercept | 53.487 | 26.750 | 2.000 | 0.0561 | |
| Altitude (m) | −0.138 | 0.269 | −0.512 | 0.6127 | |
| Angle (degrees) | 0.895 | 0.454 | 1.970 | 0.0595 | |
| Flight Pattern | −5.689 | 7.762 | −0.733 | 0.4702 | |

Significant parameters (α = 0.05) indicated in boldface.

dominant and codominant overstory trees, likely meaning our overstory extraction rate should be on the higher range of that reported in the literature. These relatively high tree extraction rates for open-canopy ponderosa pine systems are attributed to the general segregation of different size trees (Fig. 3). Within more shade tolerant forest systems with multiple overlapping canopy layers, the local-maximum extraction methods used in this study are known to miss most suppressed trees (Jeronimo et al., 2018). In comparison with a study conducted at the same study site, we saw a 0.19 increase in F-score across all tree sizes with the only difference being the use of 0.10 cm CHM as opposed to a 0.25 cm CHM by Creasy et al. (2021). This suggests that CHM resolution should be further investigated to determine its impact on tree extraction rates.

Linear regression across the 30 UAS extracted tree datasets suggests some flexibility in flight parameters for maximizing F-score, precision, and recall (Table 3). UAS acquisitions conducted using a crosshatch flight pattern paired with nadir a camera angle maximized tree detection results (Fig. 6). The indication of a nadir flight angle is counter to what has been seen in previous studies (Nesbit and Hugenholtz, 2019) that suggested 20–35° off-nadir imagery improves systematic SfM block bundle adjustment errors. We speculate that the consumer-grade GPS equipped in the DJI Phantom 4 Pro paired with the difficulty of identifying ground control points in off-nadir images led to greater miss-alignment errors compared to the nadir acquisitions. Further testing of off-nadir flight designs should explore using UAS platform with real time kinematic geolocation accuracy to reduce error through manual ground control point georegistration (Tomaštík et al., 2019).

### 4.2. UAS extracted height and DBH

The high extracted tree height $R^2$ (>0.98) found in this study exceed what has previously been reported in ponderosa pine dominated forests (0.92–0.95; Belmonte et al., 2020). Our improved height correlations compared to Belmonte et al. (2020) may be attributed to their 15 cm resolution imagery as opposed to the finer resolution used in this study (1.8 and 3.2 cm at 65 and 115 m, respectively), with our finer resolution imagery likely capturing more canopy detail. Additionally, we had generally small tree height biases (<±0.15 m) in all acquisitions, in line with, or slightly better than, accuracies reported in both UAS-SfM and

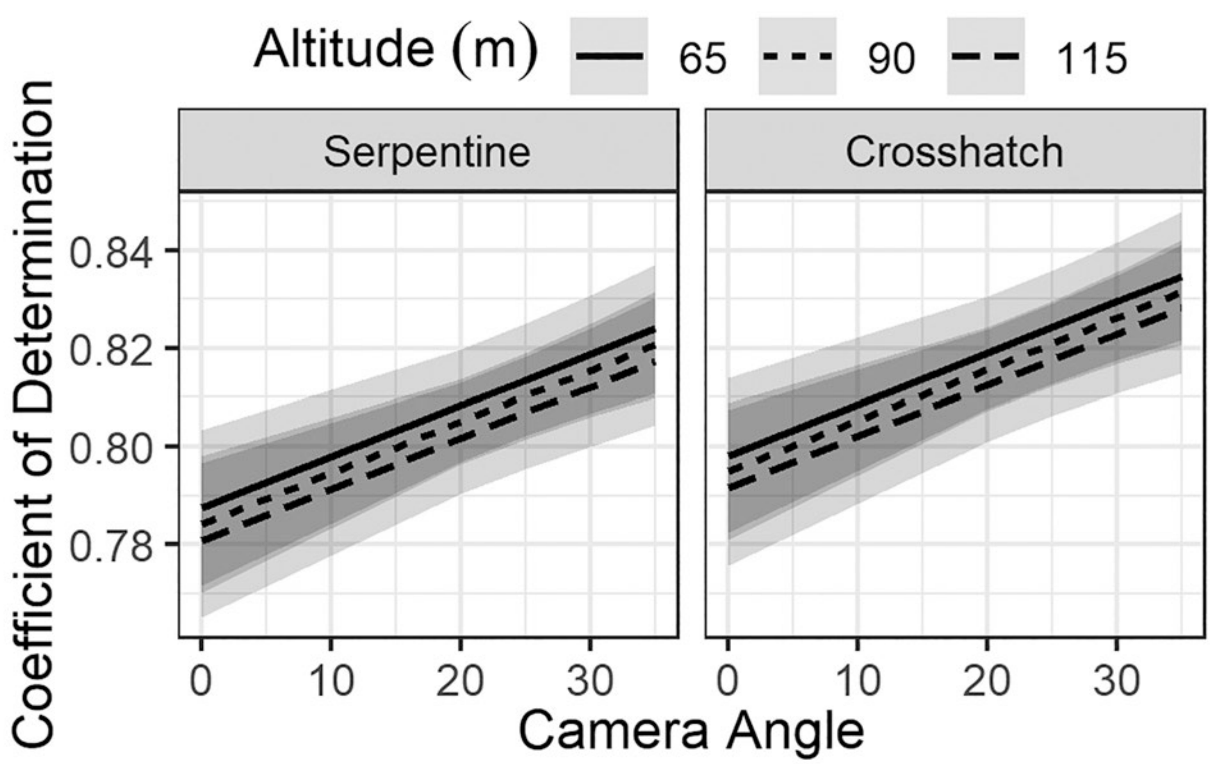


**Fig. 8.** Visualization of multiple linear regression of coefficient of determination between extracted and observed DBH values against predictors of altitude, camera angle, and flight pattern. (1-column figure).

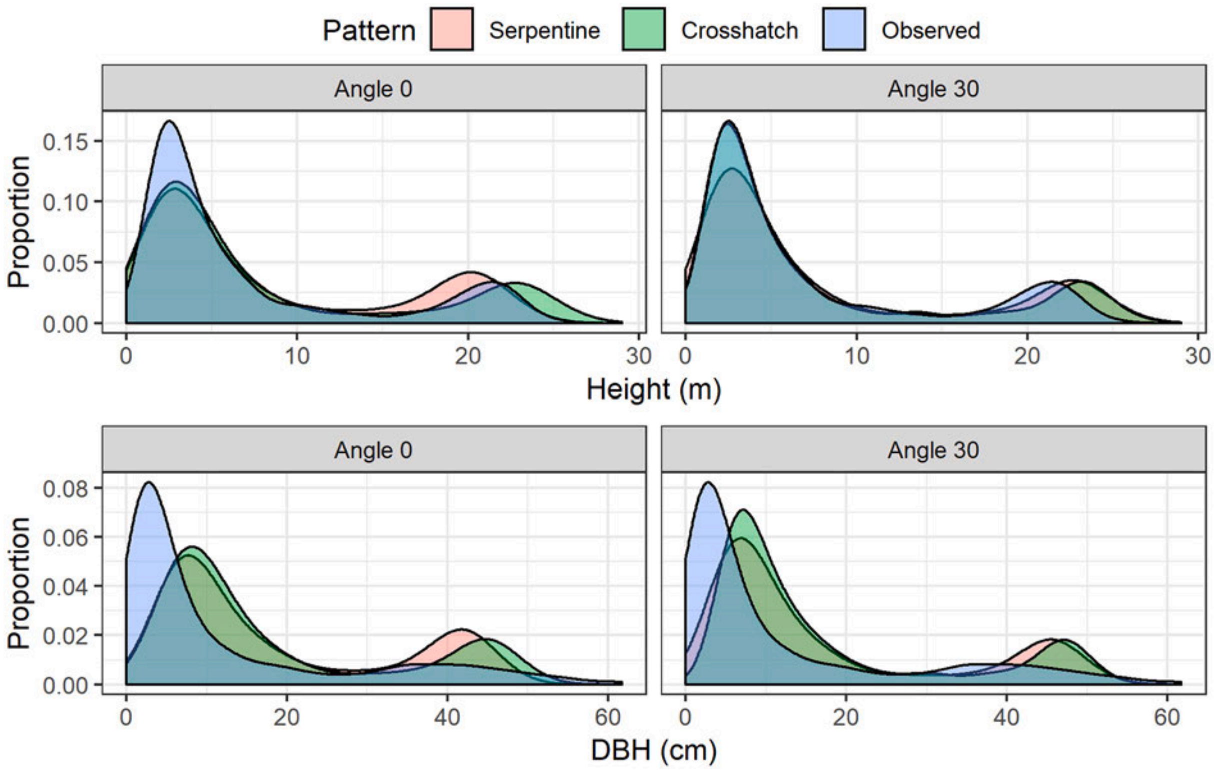


**Fig. 9.** Distributional comparison of (top) extracted tree heights and (bottom) modeled UAS DBH values from 65 m altitude acquisitions against field observed heights and DBHs. (2-column figure).

UAS-LiDAR studies (e.g., −0.13 to −0.38 m in Krause et al., 2019 and −0.69 m in Dalla Corte et al., 2020). Like in this study, assessment of remotely estimated tree heights is consistently done by comparison with field measurements from laser rangefinder that have expected RMSEs of ~10% (Vastaranta et al., 2009). In this context, UAS-derived tree heights have potential to be as precise if not more precise than their field derived counterparts. Previous work comparing independent UAS-SfM-derived surface models at the same time point in vegetation free areas found a median elevation difference of 0.03 m, with 50% of elevation differences being <0.05 m (Goetz et al., 2018). This study found errors ranging from 0.001 to 0.33 m were strongly explained by distance to ground control points, image acquisition height, and number of image view angles of the same location. To better understand the reliability of UAS-derived tree heights, future work should explore the stability of independent UAS acquisitions of the same stand as this would reveal any errors propagating from the SfM algorithm and inform the potential for repeat acquisitions for tree growth monitoring.

This study's highest extracted tree DBH rates (>40%) were achieved with crosshatch flight patterns using moderately off-nadir camera angles (25–30°) that provided more complete stem reconstruction (Fig. 5). Previous work has demonstrated how the increased overlap of crosshatch flight designs improves image registration and provides increased point densities beneath the dominant forest canopy (Dandois et al., 2015; Seifert et al., 2019). However, even our best extraction rate (47.8%) falls below that of Fritz et al. (2013) who extracted 70% of DBH values using off-nadir UAS datasets in a leaf-off deciduous forest. These results also fall in the middle of what has been achieved for UAS-LiDAR DBH extraction, which has varied between 18 and 82% of tree stems (Brede et al., 2017; Neuville et al., 2021). Our lower extraction rates are likely due to occlusion caused by the persistent coniferous canopy, resulting in lower point densities within the DBH point cloud slices than was seen in Fritz et al. (2013). However, incomplete extraction of DBHs was expected, with the hope that enough DBH values would be available for UAS modeling of the missing DBH values. It was important to consider that this study and Fritz et al. (2013) occurred in open-canopy ponderosa pine and leaf-off deciduous forests conditions, respectively, these forest conditions are expected to be more conducive to DBH extraction with this strategy likely breaking down in more closed canopy coniferous or leaf-on deciduous settings.

Filtering of the extracted heights and DBHs that were spatially matched with the FIA regional height to DBH relationship removed a substantial component of falsely extracted DBH values. Despite extracting an average of 31.1% of DBHs, only 8.1% of DBH values on average were retained through the filtering process. In considering just overstory forest structure (tree >5 tall), the best DBH extraction flight (65 m altitude; crosshatch; 25° camera angle) retained 20.5% of DBHs through the filtering process. Coefficients of determination for unfiltered extracted DBHs varied widely (0.307–0.784) with field observed DBHs across the flight designs. However, the filtering process increased $R^2$ to 0.759–0.846, with these tending to be strongest for crosshatch and off-nadir flight designs (Fig. 8). These $R^2$ values exceed the 0.484 achieved by Fritz et al. (2013) using UAS-SfM and the $R^2$ of 0.06 to 0.29 reported by Neuville et al. (2021) using UAS-LiDAR for direct DBH extraction. However, similar results have been achieved by Brede et al. (2017), with $R^2 = 0.96$ when comparing DBH values from UAS-LiDAR and TLS observations. Additionally, these accuracies fall in line with $R^2$ values reported for UAS-SfM DBH values predicted using pre-existing local height to DBH relationships (González-Jaramillo et al., 2019). This filtering process was able to remove erroneously extracted DBH values that likely resulted from partially reconstructed stems or branches within the point cloud slice, leaving an average of 72 UAS extracted DBHs in each dataset from which to generate a UAS-based height to DBH relationship. Future efforts should integrate nadir and off-nadir imagery to explore if the benefits of nadir flights for image alignment can be combined with the oblique view angles of tree crowns and stems to provide the best of both strategies for DBH extraction and modeling.

Potential sources of error in extracting individual tree locations and DBH values could result from image alignment and point cloud

Remote Sensing of Environment 263 (2021) 112540

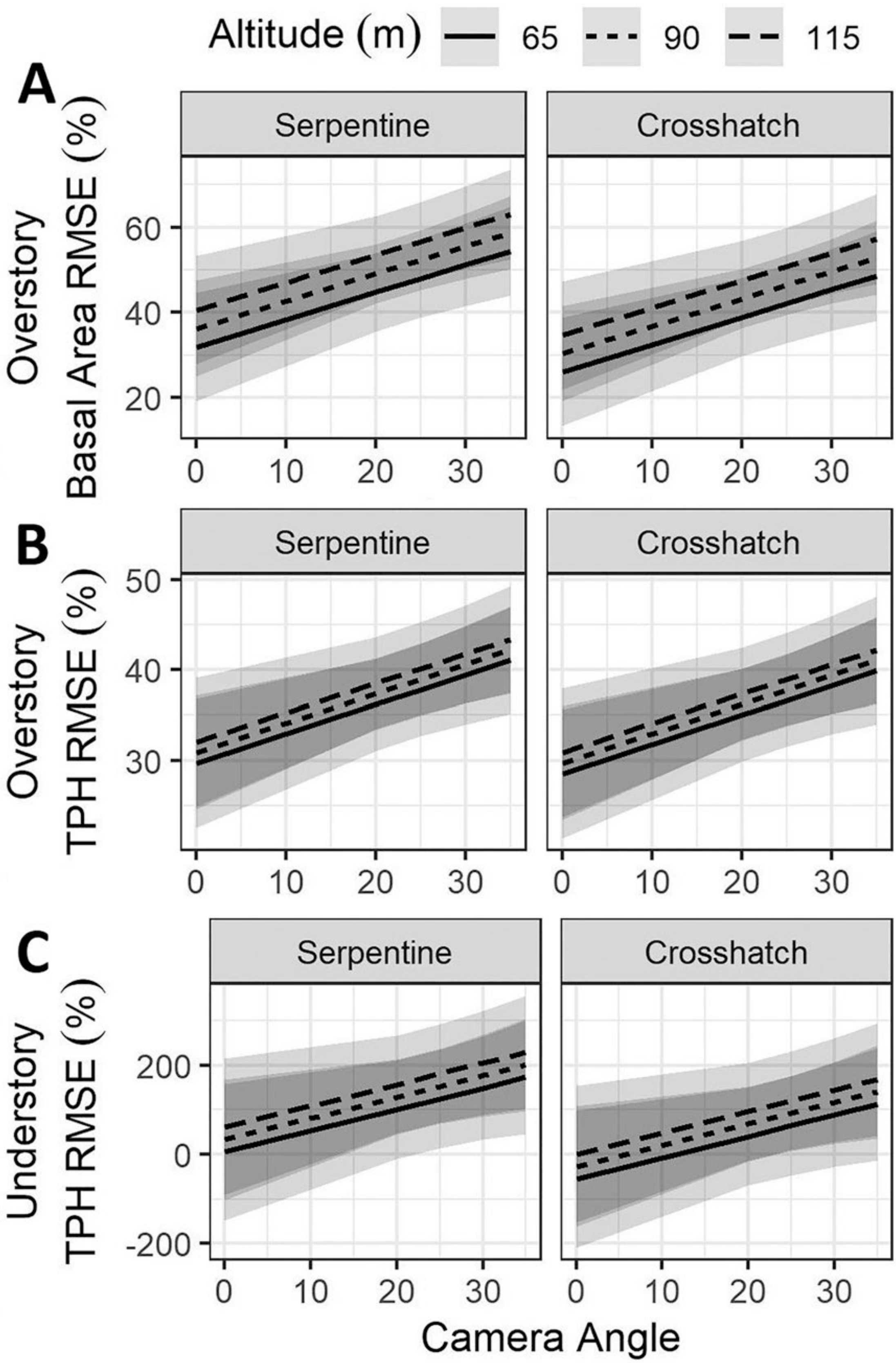


**Fig. 10.** Visualization of multiple linear regression of the response variable (A) overstory basal area RMSE (%), (B) overstory TPH RMSE (%), and (C) understory TPH RMSE (%) against predictors of altitude, camera angle, and flight pattern. (2-column figure).

**Table 5**
Multiple linear regression of UAS acquisition parameter influence on summarized extracted tree density metrics, where flight pattern was coded as serpentine = 0 and crosshatch = 1.

| Parameter | Coefficient | Standard Error | t-value | *P*-value | Adj. $R^2$ |
|---|---|---|---|---|---|
| Response = Understory TPH RMSE (%) | | | | | 0.0745 |
| Intercept | −96.98 | 145.82 | −0.665 | 0.5119 | |
| Altitude (m) | 1.11 | 1.47 | 0.759 | 0.4547 | |
| Angle (degrees) | 4.78 | 2.48 | 1.929 | 0.0647 | |
| Flight Pattern | −43.09 | 42.31 | −1.018 | 0.3179 | |
| Response = Overstory TPH RMSE (%) | | | | | 0.1609 |
| Intercept | 26.09 | 6.79 | 3.843 | 0.0007 | |
| Altitude (m) | 0.05 | 0.07 | 0.682 | 0.5013 | |
| Angle (degrees) | 0.32 | 0.12 | 2.814 | **0.0092** | |
| Flight Pattern | −0.82 | 1.97 | −0.419 | 0.6788 | |
| Response = Overstory Basal Area Hectare RMSE (%) | | | | | 0.2608 |
| Intercept | 17.69 | 12.11 | 1.460 | 0.1563 | |
| Altitude (m) | 0.17 | 0.12 | 1.423 | 0.1666 | |
| Angle (degrees) | 0.64 | 0.21 | 3.134 | **0.0042** | |
| Flight Pattern | −4.14 | 3.52 | −1.178 | 0.2496 | |

Significant parameters (α = 0.05) indicated in bold.

positional accuracy. The relatively small alignment errors visually observed in the stem point cloud slices (Fig. 5) likely propagate into the DBH extraction process and contribute to the relatively high number of DBH values that are filtered out by the regional height to DBH relationship. Similarly, the observed horizontal errors in the point cloud location (Table 2) could contribute to false or omitted matches between the extracted tree values and the stem mapped trees. However, the use of a 4 m buffer during the tree matching process was designed to account for small geolocation errors in the extracted and stem mapped trees, along with errors introduced due to tree lean off-setting the extracted tree locations.

### 4.3. Local UAS height to DBH relationships

The filtered pairs of extracted tree heights and DBHs provided a large enough sample dataset to create UAS-based height to DBH relationships for estimating missing DBH values associated with each UAS extracted tree height. The UAS predicted DBH values tended to overestimate diameters for smaller trees and underestimated the largest diameters (Fig. 9). Errors at the DBH distribution tails are somewhat expected as these values are less represented in the extracted data pairs and likely present unaccounted for variation in local growing environments. Particularly for smaller trees growing in dense environments or beneath the crowns of mature trees, they often allocate greater resources to height growth compared to DBH growth (Barrett, 1982). This is at least partially supported by other studies that have found UAS estimates of crown diameter and area to improve predictions of DBH compared to height only models (Iizuka et al., 2018). Our local UAS-based modeling of DBH could be improved by exploring other UAS-based predictors in a multiple linear regression capable of accounting for density by including metrics like delineated crown area/volume or extracted local stem density.

### 4.4. Estimations of plot- and stand-level metrics

Across all metrics of forest density (overstory and understory TPH and overstory basal area per hectare), the best performing acquisitions had plot-level correlations exceeding 0.8 with field observed density metrics. Of the tested UAS datasets, 40% had correlations exceeding 0.8 for overstory TPH (>5 m tall) and field observed TPH, with the strongest correlations coming from crosshatch and off-nadir flight designs. However, acquisitions with a 35° camera angle had correlations <0.5. Our strength in estimating overstory TPH aligns with previous studies (Bonnet et al., 2017), and indicates that the relative trend in overstory tree density was captured. However, the best performing models failed to identify two trees in each 0.04 ha plot on average, resulting in an underestimation bias of 13% or ~50 TPH.

Similar high correlations (>0.8) were found for estimates of understory TPH for all but the serpentine 35° off-nadir acquisitions. The best correlation values exceeded 0.9, with all of these being 65 m altitude acquisitions using either off-nadir or crosshatch flight designs. However, the underestimation bias of understory tree density was larger at an average of 4 trees per plot, equivalent to 20% or ~100 TPH at the stand level. This increased negative bias for understory trees aligns with the decreased probability of detecting understory trees using single tree detection strategies described in other studies (Creasy et al., 2021).

Across the 30 UAS datasets, the four top correlations exceeded 0.8 for estimates of overstory basal area per acre and were acquired at 65 m altitude with either off-nadir or crosshatch flight designs. For these high correlation datasets plot-level basal area per hectare RMSE was 27–37%. However, when summarized at the stand scale 43% of datasets estimated overstory basal area per hectare to within 10% (2.3 $m^2$ $ha^{-1}$). This high accuracy at the stand level is similar to that reported by Belmonte et al. (2020) who evaluated basal area in pre- and post-treatment ponderosa pine. This indicates that while the relative trend and stand average basal area per hectare were accurately captured, within-stand variation was spatially misaligned. Visual inspection of plot-level basal area per hectare residuals showed that the largest error terms were spatially correlated in neighboring plots, such that large positive errors were next to large negative errors. The authors take this spatially correlation in errors to indicate that small location differences between extracted and stem mapped trees might explain the relatively large plot-level RMSE.

Ranking acquisitions based on having high plot-level correlations along with minimizing stand-level error for all density metrics places seven 65 m altitude acquisitions in the top 10 datasets, with this including all five crosshatch datasets. This suggests that individual tree assessment for describing plot- and stand-level forest structure in ponderosa pine systems is best described through lower altitude UAS flights using either off-nadir or crosshatch flight designs. Our high correlation and precision in modeling overstory forest structure has potential as a tool in guiding development of ponderosa pine silvicultural prescriptions that typically aim to increase horizontal and vertical forest heterogeneity.

### 4.5. Tree-based UAS monitoring applications

The increased focus on spatial heterogeneity management objectives within dry conifer forests has elevated the need for monitoring strategies capable of describing the matrix of trees, groups of trees, and openings that comprise a stand (Tinkham et al., 2017). This study's demonstrated UAS individual tree extraction workflow could provide near-complete tree lists of locations, heights, and DBHs within low and moderate density (<1000 TPH) conifer forest systems. Having spatially informed tree-level characteristics could enable silvicultural prescription development for a range of restoration, resilience, and wildlife focused objectives.

Such tree lists would be a valuable resource for land managers planning and implementing spatially explicit silvicultural prescriptions and would enable managers to map explicit locations for tree retention and planned openings for use by marking crews. Implementing matrices of openings and tree groups through dry conifer restoration has been found to limit crown fire spread (Ziegler et al., 2017b) and reduce beetle mortality intensity by fragmenting continuity between susceptible hosts (Fettig et al., 2007). Such management strategies often target removal of understory and suppressed trees, and while our understory estimates do not reflect exact density levels, the results capture relative understory densities across the stand which could guide thinning objectives that target understory trees (Allen et al., 2002). While not all trees were successfully extracted from the UAS data, the presented methods capture both the relative local trends and stand-level averages that are necessary for informing a broad range of thinning and restoration (Almeida et al., 2019) actions in lower density forests (< ~1000 tree ha$^{-1}$) like temperate and montane pine dominated systems.

While the presented UAS methods have potential to characterize stand wide tree lists of locations, heights, and DBHs, these approaches have only been tested at a small scale (1 ha) in a relatively open-canopy ponderosa pine forest. For such approaches to be fully operationalized in land management, further testing needs to be conducted across a broader range of forest structure and species compositions. Further testing will help identify the range of forest conditions that UAS tree-based monitoring can be used to reliably inform management decisions.

## 5. Conclusions and suggestions

This study demonstrates a novel UAS-based inventory strategy for estimating individual tree structural attributes (i.e., location, height, and DBH) in dry conifer forests. We found that a crosshatch flight pattern (1) maximized UAS SfM individual tree detection rates and (2) minimized extracted tree height and DBH errors. Additionally, we found that combining crosshatch with off-nadir camera angles (3) improved UAS-based modeling of individual tree DBH and (4) provided the best representation of plot- and stand-level density metrics. Our filtering of UAS extracted DBH samples with national forest inventory data appears to provide a route for modeling individual tree DBH values, without the need for in situ field observations. Despite the high accuracy of modeled stand basal area estimates, individual tree DBH accuracy decreased for both the smallest and largest trees. Future work should explore how other UAS derived attributes like stem density, crown area, and relative height compared to neighboring trees could account for competition impacts on modeled individual tree DBHs. The spatial tree list of heights and DBHs provided by this study's UAS individual tree extraction workflow could provide the tree-level characteristics needed for silvicultural prescription development for a range of restoration, resilience, and wildlife focused objectives.

Operationalizing UAS-based individual tree inventories will require balancing data precision against characterizing broader extents (10s–100s ha). The crosshatch data acquisition conducted in this study doubled the data acquisition time, image storage requirements, and processing time to gain an estimated 5–10% improvement in UAS derived inventory products. The largest benefit of the crosshatch flight pattern came from an ~30% increase in the number of DBH values successfully extracted and matched with UAS derived tree heights compared to the serpentine pattern. However, the results make it clear that it is unrealistic to expect above canopy UAS acquisitions to capture all DBH values; i.e., UAS-based individual tree inventories might see efficiency gains by flying entire stands with serpentine patterns and then sample portions of a stand with a crosshatch pattern to improve DBH extraction rates. Work is needed to understand what proportion of a stand needs to be sampled with the crosshatch pattern to ensure enough DBH values are extracted to impute the missing DBH values.

## Declaration of Competing Interest

The authors declare that they have no known competing financial interests or personal relationships that could have appeared to influence the work reported in this paper.

## Acknowledgements

The authors would like to thank Dr. Mike Battaglia, Dr. Wayne Shepperd, and Lance Asherin for establishing and maintaining the stem mapped study site. This project was funded through USDA McIntire-Stennis appropriations to Colorado State University.

## References

Addington, R.N., Aplet, G.H., Battaglia, M.A., Briggs, J.S., Brown, P.M., Cheng, A.S., Dickinson, Y.A., Feinstein, J.A., Pelz, K.A., Regan, C.M., Thinnes, J.W., Truex, R.L., Fornwalt, P.J., Gannon, B., Julian, C.W., Underhill, J.L., Wolk, B., 2018. Principles and practices for the restoration of ponderosa pine and dry mixed-conifer forests of the Colorado Front Range. In: Gen. Tech. Rep. RMRS-GTR-373. U.S. Department of Agriculture, Forest Service, Rocky Mountain Research Station, Fort Collins, CO (121 pp.).

Allen, C.D., Savage, M., Falk, D.A., Suckling, K.F., Swetnam, T.W., Schulke, T., Stacey, P. B., Morgan, P., Hoffman, M., Klingel, J.T., 2002. Ecological restoration of southwestern ponderosa pine ecosystems: a broad perspective. Ecological App. 12 (5), 1418–1433. https://doi.org/10.1890/1051-0761(2002)012[1418:erospp]2.0.co;2.

Almeida, D.R.A., Broadbent, E.N., Zambrano, A.M.A., Wilkinson, B.E., Ferreira, M.E., Chazdon, R., Meli, P., Gorgens, E.B., Silva, C.A., Stark, S.C., Valbuena, R., 2019. Monitoring the structure of forest restoration plantations with a drone-lidar system. Int. J. Appl. Earth Obs. Geoinf. 79, 192–198.

Barrett, J.W., 1982. Twenty-Year Growth of Ponderosa Pine Saplings Thinned to Five Spacings in Central Oregon. Pacific Northwest Forest and Range Experiment Station, U.S. Dept. of Agriculture, Forest Service. https://doi.org/10.5962/bhl.title.88007.

Battaglia, M.A., Gannon, B., Brown, P.M., Fornwalt, P.J., Cheng, A.S., Huckaby, L.S., 2018. Changes in forest structure since 1860 in ponderosa pine dominated forests in the Colorado and Wyoming Front Range, UAS. For. Eco. Manag. 422, 147–160. https://doi.org/10.1016/j.foreco.2018.04.010.

Belmonte, A., Sankey, T., Biederman, J.A., Bradford, J., Goetz, S.J., Kolb, T., Woolley, T., 2020. UAV-derived estimates of forest structure to inform ponderosa pine forest restoration. Remote Sens. https://doi.org/10.1002/rse2.137.

Bonnet, S., Lisein, J., Lejeune, P., 2017. Comparison of UAS photogrammetric products for tree detection and characterization of coniferous stands. Int. J. Remote Sens. 38 (19), 5310–5337. https://doi.org/10.1080/01431161.2017.1338839.

Boyden, S., Binkley, D., Shepherd, W., 2005. Spatial and temporal patterns in structure, regeneration, and mortality of an old-growth ponderosa pine forest in the Colorado Front Range. For. Ecol. Manag. 219 (1), 43–55.

Brede, B., Lau, A., Bartholomeus, H.M., Kooistra, L., 2017. Comparing RIEGLE RiCOPTER UAV lidar derived canopy height and DBH with terrestrial lidar. Sensors 17, 2371. https://doi.org/10.3390/s17102371.

Cannon, J.B., Barrett, K.J., Gannon, B.M., Addington, R.N., Battaglia, M.A., Fornwalt, P. J., Aplet, G.H., Cheng, A.S., Underhill, J.L., Briggs, J.S., Brown, P.M., 2018. Collaborative restoration effects on forest structure in ponderosa pine-dominated forests of Colorado. For. Ecol. Manag. 424, 191–204. https://doi.org/10.1016/j.foreco.2018.04.026.

Conto, T., 2019. TreeLS: Terrestrial Point Cloud Processing of Forest Data. R package version 1.0. https://CRAN.R-project.org/package=TreeLS.

Conto, T.D., Olofsson, K., Görgens, E.B., Rodriguez, L.C.E., Almeida, G., 2017. Performance of stem denoising and stem modelling algorithms on single tree point clouds from terrestrial laser scanning. Comput. Electron. Ag 143, 165–176. https://doi.org/10.1016/j.compag.2017.10.019.

Cook, K.L., 2017. An evaluation of the effectiveness of low-cost UAVs and structure from motion for geomorphic change detection. Geomorphology 278, 195–208. https://doi.org/10.1016/j.geomorph.2016.11.009.

Creasy, M.B., Tinkham, W.T., Hoffman, C.M., Vogeler, J.C., 2021. Potential for individual tree Monitoring in ponderosa pine-dominated forests using unmanned aerial system structure from motion point clouds. Can. J. For. Res. https://doi.org/10.1139/cjfr-2020-0433.

Dalla Corte, A.P.D., Rex, F.E., de Almeida, D.R.A., Sanquetta, C.R., Silva, C.A., Moura, M. M., Wilkinson, B., Zambrano, A.M.A., da Cunha Neto, E.M., Veras, H.F.P., de Moraes, A., Klauberg, C., Mohan, M., Cardil, A., Broadbent, E.N., 2020. Measuring individual tree diameter and height using GatorEye high-density UAV-lidar in an integrated crop-livestock-forest system. Remote Sens. 12, 863. https://doi.org/10.3390/rs12050863.

Dandois, J., Olano, M., Ellis, E., 2015. Optimal altitude, overlap, and weather conditions for computer vision UAV estimates of forest structure. Remote Sens. 7 (10), 13895–13920. https://doi.org/10.3390/rs71013895.

Dandois, J.P., Ellis, E.C., 2013. High spatial resolution three-dimensional mapping of vegetation spectral dynamics using computer vision. Remote Sens. Environ. 136, 259–276. https://doi.org/10.1016/j.rse.2013.04.005.

Díaz, G.M., Mohr-Bell, D., Garrett, M., Muñoz, L., Lencinas, J.D., 2020. Customizing unmanned aircraft systems to reduce forest inventory costs: can oblique images substantially improve the 3D reconstruction of the canopy? Int. J. Remote Sens. 41 (9), 3480–3510. https://doi.org/10.1080/01431161.2019.1706200.

Falkowski, M.J., Smith, A.M.S., Hudak, A.T., Gessler, P.E., Vierling, L.A., Crookston, N.L., 2006. Automated estimation of individual conifer tree height and crown diameter via two-dimensional spatial wavelet analysis of lidar data. Can. J. Remote. Sens. 32, 153–161.

Fettig, C.J., Klepzig, K.D., Billings, R.F., Munson, A.S., Nebeker, T.E., Negrón, J.F., Nowak, J.T., 2007. The effectiveness of vegetation management practices for prevention and control of bark beetle infestations in coniferous forests of the western and southern United States. For. Ecol. Manag. 238 (1–3), 24–53. https://doi.org/10.1016/j.foreco.2006.10.011.

Forsman, M., Börlin, N., Holmgren, J., 2016. Estimation of tree stem attributes using terrestrial photogrammetry with a camera rig. Forests 7 (12), 61. https://doi.org/10.3390/f7030061.

Frey, J., Kovach, K., Stemmler, S., Koch, B., 2018. UAV photogrammetry of forests as a vulnerable process. A sensitivity analysis for a structure from motion RGB-image pipeline. J. Remote Sens. 10 (6), 912. https://doi.org/10.3390/rs10060912.

Fritz, A., Kattenhorn, T., Koch, B., 2013. UAV-based photogrammetric point clouds - tree stem mapping in open stands in comparison to terrestrial laser scanner point clouds. International Archives of the Photogrammetry. Remote Sens. Spatial Inform. Sci. XL-1, W2. https://doi.org/10.5194/isprsarchives-XL-1-W2-141-2013.

Goetz, J., Brenning, A., Marcer, M., Bodin, X., 2018. Modeling the precision of structure-from-motion multi-view stereo digital elevation models from repeated close-range aerial surveys. Remote Sens. Environ. 210, 208–216. https://doi.org/10.1016/j.rse.2018.03.013.

González-Jaramillo, V., Fries, A., Bendix, J., 2019. AGB estimation in a tropical mountain forest (TMF) by means of RGB and multispectral images using an unmanned aerial vehicle (UAV). Remote Sens. 11 (12), 1413. https://doi.org/10.3390/rs11121413.

Heinzel, J., Huber, M., 2016. Detecting tree stems from volumetric TLS data in forest environments with rich understory. Remote Sens. 9 (1), 9. https://doi.org/10.3390/rs9010009.

Hopkinson, C., Chasmer, L., Young-Pow, C., Treitz, P., 2004. Assessing forest metrics with a ground-based scanning lidar. Can. J. For. Res. 34 (3), 573–583. https://doi.org/10.1139/x03-225.

Iizuka, K., Yonehara, T., Itoh, M., Kosugi, Y., 2018. Estimating tree height and diameter at breast height (DBH) from digital surface models and orthophotos obtained with an unmanned aerial system for a Japanese cypress (*Chamaecyparis obtusa*) forest. Remote Sens. 10 (1), 13. https://doi.org/10.3390/rs10010013.

Jeronimo, S.M.A., Kane, V., Churchill, D.J., McGaughey, R., Franklin, J.F., 2018. Applying LiDAR individual tree detection to management of structurally diverse forest landscapes. J. Forestry 116 (4), 336–346. https://doi.org/10.1093/jofore/fvy023.

Kandare, K., Ørka, H.O., Chan, J.C.-W., Dalponte, M., 2016. Effects of forest structure and airborne laser scanning point cloud density on 3D delineation of individual tree crowns. European J. Remote Sens. 49 (1), 337–359. https://doi.org/10.5721/eujrs20164919.

Krause, S., Sanders, T.G., Mund, J.-P., Greve, K., 2019. UAV-based photogrammetric tree height measurement for intensive forest monitoring. Remote Sens. 11 (7), 758. https://doi.org/10.3390/rs11070758.

Liang, X., Jaakkola, A., Wang, Y., Hyyppä, J., Honkavaara, E., Liu, J., Kaartinen, H., 2014. The use of a hand-held camera for individual tree 3D mapping in forest sample plots. Remote Sens. 6 (7), 6587–6603. https://doi.org/10.3390/rs6076587.

Maas, H.G., Bienert, A., Scheller, S., Keane, E., 2008. Automatic forest inventory parameter determination from terrestrial laser scanner data. Int. J. Remote Sens. 29 (5), 1579–1593. https://doi.org/10.1080/01431160701736406.

Mikita, T., Janata, P., Surový, P., 2016. Forest stand inventory based on combined aerial and terrestrial close-range photogrammetry. Forests 7 (8), 165. https://doi.org/10.3390/f7080165.

Mohan, M., Silva, C., Klauberg, C., Jat, P., Catts, G., Cardil, A., Hudak, A., Dia, M., 2017. Individual tree detection from unmanned aerial vehicle (UAV) derived canopy height model in an open canopy mixed conifer forest. Forests 8 (9), 340. https://doi.org/10.3390/f8090340.

Mokroš, M., Liang, X., Surový, P., Valent, P., Čerňava, J., Chudý, F., Tunák, D., Saloň, Š., Merganič, J., 2018. Evaluation of close-range photogrammetry image collection methods for estimating tree diameters. ISPRS Int. J. Geo-Inform. 7 (3), 93. https://doi.org/10.3390/ijgi7030093.

Nesbit, P., Hugenholtz, C., 2019. Enhancing UAV–SfM 3D model accuracy in high-relief landscapes by incorporating oblique images. Remote Sens. 11 (3), 239. https://doi.org/10.3390/rs11030239.

Neuville, R., Bates, J.S., Jonard, F., 2021. Estimating forest structure from UAV-mounted lidar point cloud using machine learning. Remote Sens. 13, 352. https://doi.org/10.3390/res13030352.

Nilsson, M., 1996. Estimation of tree heights and stand volume using an airborne lidar system. Remote Sens. Environ. 56 (1), 1–7. https://doi.org/10.1016/0034-4257(95)00224-3.

North, M., Stine, P., O'Hara, K., Zielinski, W., Stephens, S., 2009. An ecosystem management strategy for Sierra mixed-conifer forests. In: Gen. Tech. Rep. PSW-GTR-220. U.S. Department of Agriculture, Forest Service, Pacific Southwest Research Station, Albany, CA (49 pp.).

Paris, C., Kelbe, D., Aardt, J.V., Bruzzone, L., 2017. A novel automatic method for the fusion of ALS and TLS LiDAR data for robust assessment of tree crown structure. IEEE Trans. Geosci. Remote Sens. 55 (7), 3679–3693. https://doi.org/10.1109/tgrs.2017.2675963.

Piermattei, L., Karel, W., Wang, D., Wieser, M., Mokroš, M., Surový, P., Koreň, M., Tomaštík, J., Pfeifer, N., Hollaus, M., 2019. Terrestrial structure from motion photogrammetry for deriving forest inventory data. Remote Sens. 11 (8), 950. https://doi.org/10.3390/rs11080950.

Pinheiro, J., Bates, D., DebRoy, S., Sarkar, D., 2018. Nlme: Linear and Nonlinear Mixed Effects Models. R package version 3.1-137. https://CRAN.R-project.org/package=nlme.

Plowright, A., 2018. ForestTools: Analyzing Remotely Sensed Forest Data. R package version 0.2.0. https://CRAN.R-project.org/package=ForestTools.

Popescu, S.C., Wynne, R.H., 2004. Seeing the trees in the forest. Photogram. Engine. Remote Sens. 70 (5), 589–604. https://doi.org/10.14358/pers.70.5.589.

R Core Team, 2019. R: A Language and Environment for Statistical Computing. R Foundation for Statistical Computing, Vienna, Austria.

Reynolds, R.T., Meador, A.J.S., Youtz, J.A., Nicolet, T., Matonis, M.S., Jackson, P.L., DeLorenzo, D.G., Graves, A.D., 2013. Restoring composition and structure in Southwestern frequent-fire forests: a science-based framework for improving ecosystem resiliency. In: Gen. Tech. Rep. RMRS-GTR-310. U.S. Department of Agriculture, Forest Service, Rocky Mountain Research Station, Fort Collins, CO (76 pp.).

Roussel, J.R., Auty, D., 2019. lidR: Airborne LiDAR Data Manipulation and Visualization for Forestry Applications. R package version 2.0.2. https://CRAN.R-project.org/package=lidR.

Saarinen, N., Kankare, V., Vastaranta, M., Luoma, V., Pyörälä, J., Tanhuanpää, T., Liang, X., Kaartinen, H., Kukko, A., Jaakkola, A., Yu, Xiaowei, Holopainen, M., Hyyppä, J., 2017. Feasibility of Terrestrial laser scanning for collecting stem volume information from single trees. ISPRS J. Photogram. Remote. Sens. 123, 140–158. https://doi.org/10.1016/j.isprsjprs.2016.11.012.

Sačkov, I., Kulla, L., Bucha, T., 2019. A comparison of two tree detection methods for estimation of forest stand and ecological variables from airborne LiDAR data in central European forests. Remote Sens. 11 (12), 1431. https://doi.org/10.3390/rs11121431.

Sankey, T., Donager, J., McVay, J., Sankey, J.B., 2017. UAV lidar and hyperspectral fusion for forest monitoring in the southwestern USA. Remote Sens. Environ. 195, 30. https://doi.org/10.1016/j.rse.2017.04.007.

Seifert, E., Seifert, S., Vogt, H., Drew, D., Aardt, J.V., Kunneke, A., Seifert, T., 2019. Influence of drone altitude, image overlap, and optical sensor resolution on multi-view reconstruction of forest images. Remote Sens. 11 (10), 1252. https://doi.org/10.3390/rs11101252.

Silva, C.A., Hudak, A.T., Vierling, L.A., Loudermilk, E.L., O'Brien, J.J., Hiers, J.K., Jack, S.B., Gonzalez-Benecke, C., Lee, H., Falkowski, J.M., Khosravipour, A., 2016. Imputation of individual longleaf pine (*Pinus palustris* Mill.) tree attributes from field and LiDAR data. Can. J. Remote. Sens. 42 (5), 554–573. https://doi.org/10.1080/07038992.2016.1196582.

Thiel, C., Schmullius, C., 2016. Comparison of UAV photograph-based and airborne Lidar-based point clouds over forest from a forestry application perspective. Int. J. Remote Sens. 38 (8–10), 2411–2426. https://doi.org/10.1080/01431161.2016.1225181.

Tinkham, W.T., Swayze, N.C., 2021. Influence of Agisoft Metashape parameters on UAS structure from motion individual tree detection from canopy height models. Forests 12 (2), 250. https://doi.org/10.3390/f12020250.

Tinkham, W.T., Smith, A.M.S., Affleck, D.L.R., Saralecos, J.D., Falkowski, M.J., Hoffman, C.M., Hudak, A.T., Wulder, M.A., 2016. Development of height-volume relationships in second growth Abies grandis for use with aerial LiDAR. Can. J. Remote. Sens. 42 (5), 400–410. https://doi.org/10.1080/07038992.2016.1232587.

Tinkham, W.T., Dickinson, Y., Hoffman, C.M., Battaglia, M.A., Ex, S., Underhill, J., 2017. Visualization of heterogeneous forest structures following treatment in the southern Rocky Mountains. In: Gen. Tech. Rep. RMRS-GTR-365. U.S. Department of Agriculture, Forest Service, Rocky Mountain Research Station, Fort Collins, CO (72 pp.).

Tinkham, W.T., Mahoney, P.R., Hudak, A.T., Domke, G.M., Falkowski, M.J., Woodall, C.W., Smith, A.M.S., 2018. Applications of the United States Forest Inventory and Analysis dataset: a review and future directions. Can. J. For. Res. 48 (11), 1251–1268. https://doi.org/10.1139/cjfr-2018-0196.

Tomaštík, J., Mokroš, M., Surový, P., Grznárová, A., Merganič, J., 2019. UAV RTK/PPK method—an optimal solution for mapping inaccessible forested areas? Remote Sens. 11 (6), 721. https://doi.org/10.3390/rs11060721.

Torresan, C., Berton, A., Carotenuto, F., Chiavetta, U., Miglietta, F., Zaldei, A., Gioli, B., 2018. Development and performance assessment of a low-cost UAV laser scanner system (LasUAV). Remote Sens. 10, 1094. https://doi.org/10.3390/rs10071094.

Vastaranta, M., Melkas, T., Holopainen, M., Kaartinen, H., Hyyppa, J., Hyyppa, H., 2009. Laser-based field measurements in tree-level forest data acquisition. Photo. J. Finland 21 (2), 51–61.

Venables, W.N., Ripley, B.D., 2002. Modern Applied Statistics with S, 4th ed. Springer, New York, New York, UAS (ISBN 0-387-95457-0).

Weiskittle, A.R., Hann, D.W., Kershaw Jr., J.A., Vanclay, J.K., 2011. Forest Growth and Yield Modeling. Wiley-Blackwell, West Sussex, UK, p. 424.

Wilkes, P., Jones, S.D., Suarez, L., Haywood, A., Mellor, A., Woodgate, W., Soto-Berelov, M., Skidmore, A.K., 2015. Using discrete-return airborne laser scanning to quantify number of canopy strata across diverse forest types. Methods Ecol. Evol. 7 (6), 700–712. https://doi.org/10.1111/2041-210x.12510.

You, L., Tang, S., Song, X., Lei, Y., Zang, H., Lou, M., Zhuang, C., 2016. Precise measurement of stem diameter by simulating the path of diameter tape from terrestrial laser scanning data. Remote Sens. 8 (9), 717. https://doi.org/10.3390/rs8090717.

Ziegler, J., Hoffman, C., Fornwalt, P., Sieg, C., Battaglia, M., Chambers, M., Iniguez, J., 2017a. Tree regeneration spatial patterns in ponderosa pine forests following stand-replacing fire: influence of topography and neighbors. Forests 8 (10), 391. https://doi.org/10.3390/f8100391.

Ziegler, J.P., Hoffman, C., Battaglia, M., Mell, W., 2017b. Spatially explicit measurements of forest structure and fire behavior following restoration treatments in dry forests. For. Ecol. Manag. 386, 1–12. https://doi.org/10.1016/j.foreco.2016.12.002.